UNIVERSITY OF OKLAHOMA
GRADUATE COLLEGE

SYNTHESIS OF FOLIC ACID CONJUGATED GRAPHENE QUANTUM DOT-HEXAGONAL BORON NITRIDE NANOCOMPOSITES FOR TARGETED CANCER CELL DETECTION

A THESIS
SUBMITTED TO THE GRADUATE FACULTY
in partial fulfillment of the requirements for the
Degree of
MASTER OF SCIENCE

By
SERANA NELSON
Norman, Oklahoma
2024

Downloaded from SHAREOK. Persistent Handle URL: https://hdl.handle.net/11244/340546

SYNTHESIS OF FOLIC ACID CONJUGATED GRAPHENE QUANTUM DOT-HEXAGONAL BORON NITRIDE NANOCOMPOSITES FOR TARGETED CANCER CELL DETECTION

A THESIS APPROVED FOR THE
STEPHENSON SCHOOL OF BIOMEDICAL ENGINEERING

BY THE COMMITTEE CONSISTING OF

Dr. Tahrima Rouf, Chair
Dr. Stefan Wilhelm
Dr. Qinggong Tang

© Copyright by SERANA NELSON 2024
All Rights Reserved.

Table of Contents

Acknowledgements ..... *vi*

List of Tables ..... *viii*

List of Figures ..... *ix*

Abstract ..... *x*

Chapter 1: Introduction *12*

Overview of cancer **12**

Current Diagnostic Strategies **12**

SERS: Surface Enhanced Raman Spectroscopy **13**

GQDs: Graphene quantum dots **14**

HBN: Hexagonal boron nitride **17**

GQBN: Hexagonal boron nitride-graphene quantum dots **18**

FA-GQBN: Folic acid-conjugated GQBNs **19**

Chapter 2: Scope of Thesis *20*

Hypothesis **21**

Aim 1: Optimize the fabrication and characterization of GQDs from organic rice grains. **21**

Aim 2: Optimize the fabrication and characterization of GQBN nanocomposites. **21**

Aim 3: Optimize the fabrication and characterization of FA-GQBN nanocomposites and apply them as SERS labels. **21**

Chapter 3: Materials and Methods *22*

GQD synthesis **24**

GQBN synthesis **25**

FA-GQBN synthesis **26**

Chapter 4: Results and Discussion *27*

GQD, HBN, and GQBN Physicochemical Characterizations **27**

DLS and Zeta Potential Measurements 27

SEM 29

TEM 30

FTIR 32

Raman Spectroscopy 34

XTT Biocompatibility Assay 36

Folic Acid and FA-GQBN Physicochemical Characterizations **41**

DLS 41

SEM 42

FTIR 43
Raman Spectroscopy 44
XTT Biocompatibility Assay 45
SERS of FR+ and FR- Cancer Cells 46
Chapter 5: Conclusions 50
Future Directions 51
Bibliography 52

Acknowledgements

Thank you Dr. Rouf for the opportunity to work with you and conduct this research. I want to sincerely thank my committee for their help and support in the completion of this thesis. To the Detamore, Wilhelm, and Clegg Labs, thank you so much for taking me in as one of your own. I would not have made it this far without your help. Rana, Jacob, Emi, and Dr. Clegg were instrumental in my success in this program. I learned everything I know from you all. Special thanks to the Detamore Lab Manager Peggy O'Keefe, without whom I would be lost. Thank you to my lab mates and my undergraduates Ridwan, Aimen, Airyel, Abbie, Isabella, and Jessica; you all made my job easy and kept me sane! Thank you for being so reliable and for being so cool.

This research is dedicated to the little girl who dreamt of being an engineer, only to be told time and again "girls don't make good engineers". This research is dedicated to my hopeless, broken, traumatized, and lost nineteen-year old self who never imagined I would make it this far in life much less in academia. In 2006 after the unexpected and traumatic loss of my mother to a drug overdose, I flunked out of OU. Ten years ago, I began pulling myself out of the deep, dark hole in which I found myself. I would take long runs around campus, making it a point to run by the SRTC nearly every day. I desperately yearned to be a biomedical engineer conducting research with the country's best scientists. It was then I decided I would do whatever it took to achieve my dream. Sitting at my desk in the SRTC, I still pinch myself when I realize how far I have come. Thank you to my dad, who never gave up on me. In my darkest days he loved me when I was incapable of loving myself. Thank you to my twin sister Christina. My biggest cheerleader, my best friend, and my number one supporter. Watching her success as an officer in the

Army inspires me every day. The love her soldiers have for her serves as a testament to her leadership. Her empathy, fortitude, and humility touch everyone she meets. Everything I know about leadership and gumption are thanks to her. Finally, thank you to the University of Oklahoma and SBME for taking a chance on a thirty-something college dropout. This school, this program, staff, and my colleagues allowed me to discover myself. Thanks to this university I know who I am and for the first time in my life I can confidently claim I am proud of the person I am today. I am so incredibly grateful.

List of Tables

Table 1. 3-hour XTT Cell Viability Percent Increases. _____ *40*
Table 2. 24-hour XTT Cell Viability Percent Increases. _____ *41*

List of Figures

Figure 1. Illustrative depiction of a typical SERS NP along with images of cancer imaging applications with (i) SERS imaging of a single MCF-7 human breast cancer cell; taken from Nima et al. with permission (2014). 2014, Nature Publishing Group, copyright. (ii) Ex vivo SERS imaging of tumor tissue; taken from Wang et al. with permission (2016). 2016 Nature Publishing Group copyright. (iii) In vivo SERS imaging of an intravenously injected tumor at two distinct sites. 14
Figure 2. Schematic for green synthesis of GQDs from rice. Briefly, rice is ground into a fine powder, heated at 200°C, sonicated, and then dialyzed for 4 days to obtain a solution of GQDs. 25
Figure 3. Photograph of (from left to right) commercial GQDs, synthesized GQDs, commercial GQBN, synthesized GQBN, and HBN powder. 28
Figure 4. DLS and zeta potential measurements. (A) GQD nanoparticle diameter and size distribution. (B) GQBN nanoparticle diameter and size distribution. Colored bars for 1A and 1B represent measured mean hydrodynamic dimeter, error bars show standard deviation for n = 3 replicates. (C) Zeta Potential measurements. Colored bars in 1C represent measured mean zeta potential values, error bars represent standard deviation for n= 3 replicates. 29
Figure 5. SEM images of GQBNs. (A) Disc-like structures representative of HBN nanosheets. (B) HBN nanosheets with GQDs surrounding the surface, indicated by white arrows. (C) Higher magnification imaging of GQBNs. (D) EDS image obtained from (C) but with ColorSEM; blue and green colors correspond to the GQDs. Scale bar = 1 µm. 30
Figure 6. (A) HR-TEM image of GQDs showing lattice fringes. Scale bar = 10 nm. (B) Diffraction pattern of the GQBN particle at 30 cm. (C) Bright-field TEM of GQBN particle. Scale bar = 100 nm. (D) Dark-field TEM of the same GQBN particle. Scale bar = 100 nm. 32
Figure 7. FTIR spectra for GQDs, HBN, and GQBNs. (A) FTIR spectra for GQDs. (B) FTIR spectra for HBN powder. (C) FTIR spectra for GQBN nanocomposites. 34
Figure 8. Raman spectra of (A) HBN powder, (B) GQDs and (C) GQBNs. 36
Figure 9. 3-hour XTT cell viability assay results. Colored bars represent the measured mean cell viability normalized to the cell only group. Error bars represent the standard deviation for n = 6 replicates, asterisks denote significance. Asterisk (*) denotes significance based on two-tailed t-test. 39
Figure 10. 24-hour XTT assay results. Colored bars represent the measured mean cell viability normalized to the cell only group. Error bars represent the standard deviation for n = 6 replicates, asterisks denote significance. Single asterisk (*) denotes significance based on two-tailed t-test. Double asterisk (**) denotes significance based on one-way ANOVA. 40
Figure 11. Nanoparticle diameters of (A) Folic acid in PBS, (B) GQBN nanocomposites, and (C) FA-GQBNs. Colored bars represent measured mean hydrodynamic dimeter, error bars show standard deviation for n = 3 replicates 42
Figure 12. SEM imaging of the FA-GQBN particle. (A) FA-GQBN particle in solution and (B) EDS of (A) with ColorSEM overlay. Scale bar = 1 µm and 2 µm respectively. (C) SEM of a different FA-GQBN particle in solution, and (D) Zoomed in image of particle from (C). Scale bar = 4 µm and 1 µm, respectively. 43
Figure 13. FTIR spectra of (A) Folic acid in PBS and (B) FA-GQBN particle. 44
Figure 14. Raman spectra for (A) folic acid in PBS and (B) FA-GQBNs. 45
Figure 15. XTT cell viability assay results. (A) 3-hour XTT results and (B) 24-hour XTT assay results. 24-hour XTT assay results. Black and gray bars represent the measured mean cell viability normalized to the cell only group. Error bars represent the standard deviation for n = 6 replicates. 46
Figure 16. Surface enhanced Raman spectroscopy of FR- and FR+ cancer cells. (A) Spectrum for A549 cells only. (B) Raman spectrum for A549 cells incubated with GQDs. (C) Raman spectrum for A549 cells incubated with FA-GQBNs. (D) Raman spectrum for HEC1A cells only. (E) Raman spectrum for HEC1A cells incubated with GQDs. (F) Raman spectrum for HEC1A cells incubated with FA-GQBN particles. 49

Abstract

The field of nanomedicine has evolved exponentially over the last decade with the development of new imagining modalities, nanoparticle types, and drug delivery systems aimed at treating and diagnosing cancer. Unfortunately, the paradigm for cancer diagnosis and treatment remains incomplete; there is a need for versatile and modular nanomaterials that act as contrast agents for the detection and characterization of pathologies. In this study, folic acid-conjugated graphene quantum dot-hexagonal boron nitride nanocomposites (FA-GQBNs) were synthesized for use as surface enhanced Raman spectroscopy (SERS) labels. Raman spectroscopy is a robust, label-free, spectroscopic technique that provides a molecular fingerprint and is commonly used for identifying unknown samples or compounds. Graphene quantum dots (GQDs) were synthesized from rice and bonded to hexagonal boron nitride (HBN) through electrostatic interactions. Next, graphene quantum dot-hexagonal boron nitride nanocomposites (GQBNs) are efficiently, inexpensively, and quickly synthesized using a bottom-up green synthesis strategy. Finally, to specifically and selectively target the folate receptor overexpressed on breast and gynecological cancer cells, folic acid (FA) was precisely conjugated to GQBNs to form FA-GQBNs. The synthesized nanocomposites were characterized using SEM, TEM, DLS, UV-Vis spectroscopy, FTIR, and Raman. The GQBNs were shown to increase cell proliferation by up to 36% when compared to the cell only group in cell viability assays while exhibiting superior optical and fluorescent properties and the FA-GQBNs were proven to be biocompatible. The FA-GQBNs were extensively characterized and their use as *in vitro* SERS labels as well as fluorescent labels explored. Understanding the properties and interactions of these nanocomposites

provides a foundation for developing cancer therapeutics, drug delivery systems, wound-healing hydrogels, neurological treatments, and surface enhanced Raman spectroscopy nanoparticles that could be applied in the field of nanomedicine.

Chapter 1: Introduction

Overview of cancer

Cancer continues to be one of the largest challenges facing modern medicine. A disease characterized by abnormal, uncontrollable cell growth, as well as an extremely heterogeneous microenvironment, there is an urgent need for more precise and accurate techniques for diagnosis, treatment, and monitoring. While there have been several advances in the field of cancer research in the twenty-first century, there are many challenges that remain. Among these challenges, accurate and early diagnosis for the many different types of cancer is currently one of the most urgently studied problems, as it is vital to patient outcomes and survival [1]. As one of the deadliest forms of gynecologic cancers, it is imperative to address the urgent need for novel, non-invasive, rapid breast cancer detection methods due to its high prevalence and the necessity for early intervention. Until recently, disparities in women's reproductive health and health research have plagued the scientific community[2–5]. Work is underway to address these shortcomings and this research aims to assist in filling these gaps in the research.

Current Diagnostic Strategies

Current diagnostic tools and imaging techniques are accurate but suffer from poor sensitivity which hinders early diagnosis[6]. The pathological techniques are costly and time-intensive, thus revealing an urgent need for cancer detection that is a fast, accurate, highly sensitive and selective screening method on the cellular level[1]. Because cancer is a broad disease that possesses a multitude of biomarkers, symptoms, tissue types, and

clinical presentation, a multifaceted approach for diagnostics is necessary to ensure accurate and timely diagnosis, treatment, and monitoring. An emerging strategy for the diagnosis and monitoring of cancer is surface enhanced Raman spectroscopy (SERS).

SERS: Surface Enhanced Raman Spectroscopy

SERS is based on a phenomenon called Raman scattering. First discovered by Indian physicist C.V. Raman in 1928, Raman scattering describes the unique interactions of light with matter [7–9]. SERS is an analytical technique with potent multiplexing abilities that enhances Raman signals through noble metal-based, metal oxide-based, or hybrid nanoparticles. It finds applications in materials science, analytical chemistry, trace detections, chemical sensors, food safety, and biochemistry. This is achieved by leveraging the characteristic vibrational fingerprint spectrum for in situ detection analysis [10–16]. SERS offers excellent sensitivity (up to 10^{-15} M), high signal-to-background ratio, specific fingerprint signatures, photostability, and strong multiplexing capabilities [17]. Figure 1 depicts an illustrative graphical outline of representative examples of a SERS encoded NP and its applications in cancer characterization. SERS nanoparticles can be customized in a near-infinite number of ways to detect specific particles in a sample. It is this modularity, combined with Raman spectroscopy's rich structural specificity, experimental adaptability, and extraordinarily high sensitivity made possible by the optical signal's amplification by precisely adjusted plasmonic nanostructures that makes this method an exciting and powerful tool in cancer diagnostics [1]. SERS can be used to detect circulating cancer cells, single cancer cells, and tumor microenvironment; it can be used for liquid biopsy as well as multimodal imaging [18,19], cancer cell imaging [20], targeting

cancer cells [7,8], 3D cell imaging [8], component analysis [21,22,22], assisting in tumor resection/excision [23], and more recently, theranostics [17]. Noble metals are most commonly used as SERS nanoparticles, followed by metal oxides. Recently, graphene quantum dots have garnered interest for their use as SERS NPs.

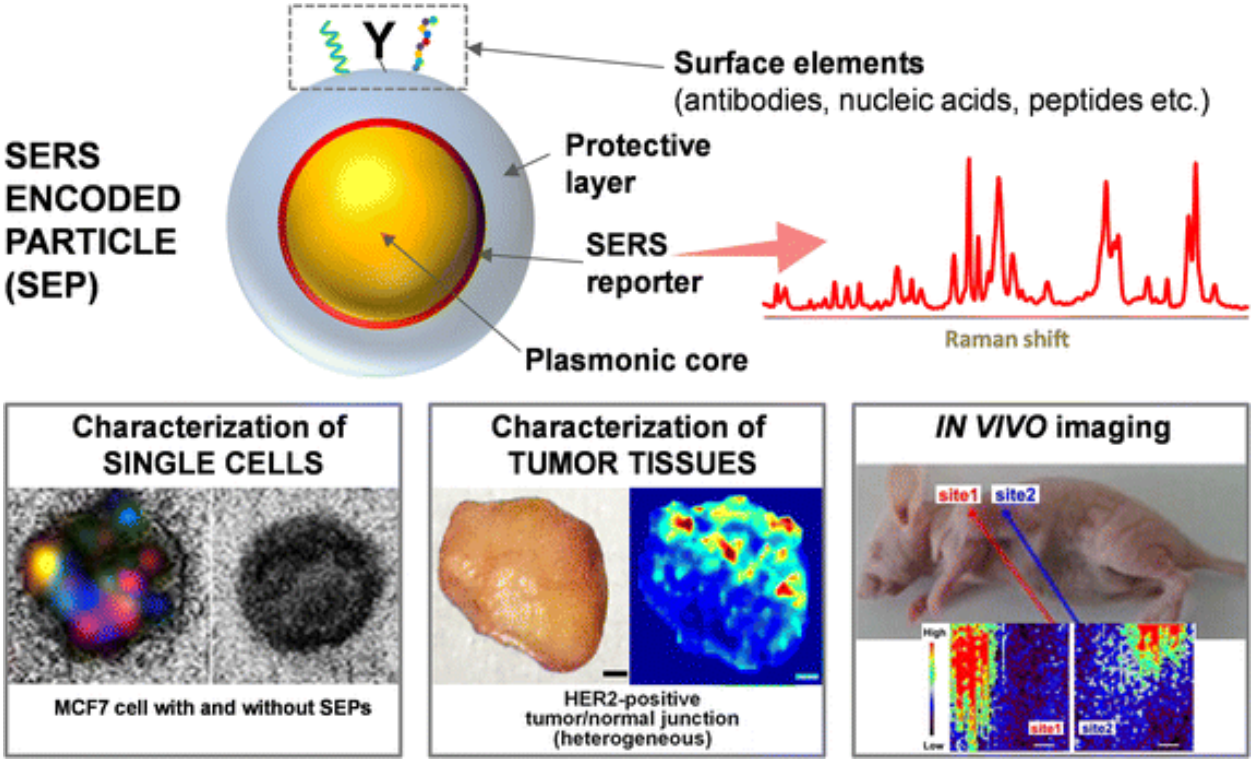

Figure 1. Illustrative depiction of a typical SERS NP along with images of cancer imaging applications with (i) SERS imaging of a single MCF-7 human breast cancer cell; taken from Nima et al. with permission (2014). 2014, Nature Publishing Group, copyright. (ii) Ex vivo SERS imaging of tumor tissue; taken from Wang et al. with permission (2016). 2016 Nature Publishing Group copyright. (iii) In vivo SERS imaging of an intravenously injected tumor at two distinct sites.

GQDs: Graphene quantum dots

Graphene quantum dots (GQDs) first emerged in 2008 and have recently been gaining momentum in a variety of applications, including drug delivery, bioimaging, neuroimaging, and wound healing[24–26]. GQDs are a zero-dimensional organic material from a class of

carbon nanomaterials called carbon dots[27]. The quantum confinement effect characteristic of GQDs produces a non-zero bandgap, while their large edge effects and amphiphilic nature give them excellent dispersibility[24,28]. Additionally, GQDs demonstrate size-dependent fluorescence emission, which enables stable, multicolor imaging under a single excitation wavelength[29]. Compared to graphene and other carbon-based materials, GQDs possess ultra-fine particle size and very large specific surface area, which enables them to accommodate more active sites for edges, functional groups, ligands, dopants, etc.[24,28]. Additionally, GQDs have highly tunable physicochemical properties, good chemical stability, low toxicity, stable photoluminescence, and high surface grafting which make them exceptional candidates for biomedical applications as well as applications for high performance electronic, photonic, and energy-related devices[24,30]. The tunable bandgap and conductivity characteristic of GQDs makes them an ideal nanoparticle for use in surface enhanced Raman spectroscopy (SERS), as it ensures excitation in the visible or near-infrared range, enables multiplexed detection, while allowing the researcher to tailor plasmon resonances[31–33]. SERS is a simple, non-destructive, quick, and label-free imaging technique with multiplexing capabilities used for biological and elemental analysis[32]. GQDs have been identified as an ideal SERS nanoparticle due to their Raman signal enhancement which results from their localized surface plasmon resonance[32].

Numerous fabrication techniques have been employed to create GQDs, including both top-down and bottom-up approaches[30]. In top-down GQD synthesis bulk carbon materials like graphene, carbon black, etc. are broken down into smaller materials through chemical/electrochemical exfoliation, hydrothermal/solvothermal treatment, or

microwave/ultrasound assisted exfoliation to produce nanoscale materials[30]. Top-down strategies can be used for mass production as there are an abundance of precursor materials and the technique is straight-forward, however, it leads to poor control over the size distribution and morphology of the final products as well as a low quantum yield[27,30]. Bottom-up synthesis strategies are based on the gradual growth and crystallization of organic precursor molecules into nanosized GQDs through thermal treatments including carbonization, pyrolysis, stepwise organic synthesis, cage opening, and chemical vapor deposition[30]. The bottom-up approach offers better control over the size of GQDs, however, fabricating high-quality, single-layer GQDs with a narrow size distribution remains a challenge[30]. Most reported synthesis strategies suffer from long reaction times, low product yields, low quantum yields, and rely on the use of harsh, corrosive chemicals[30].

There are several more challenges hindering GQDs from being widely used in biomedical applications. One of the main challenges is that GQDs are difficult to synthesize in a controlled and reproducible manner[24]. This makes it difficult to produce GQDs with consistent properties, which is essential for their use in biomedical applications. Another challenge is that GQDs are unstable in aqueous environments[24]. This makes it challenging to use them in biological systems, where aqueous conditions are the norm. Additionally, GQDs, especially those synthesized with toxic chemicals, suffer from cytotoxicity which further limits their use in medical applications[24]. Finally, the optical properties of GQDs are not as well-studied as those of other quantum dot materials, which can make it difficult to predict how they will behave in biological environments[24].

There are a few green synthesis approaches for GQDs, including GQDs from biomass waste, coffee grounds, and white rice[34], [35], [36]. While these studies are useful, there is still a knowledge gap regarding in-depth analysis of green synthesis of GQDs that not only sheds light into the complex mechanism of GQD production but also ensures large scale reproducibility with consistent properties for biomedical applications. Moreover, the predominant edges and dangling bonds present in GQDs can make their stability a challenge and reveals the need for a stabilizing compound in order to fully exploit the unique properties of this nanoscale material[37]. One promising material for imparting chemical stability to GQDs is hexagonal boron nitride [38].

HBN: Hexagonal boron nitride

Hexagonal boron nitride (HBN) nanosheets are a two-dimensional, ultrathin layered material that have become a desirable compound for applications in drug delivery, biosensors, and tissue engineering due to its remarkable properties which include self-assembly, biocompatibility, high mechanical strength, large thermal conductivity, and a low dielectric constant[39,40]. The crystal structure of BN materials are similar to graphene, however, BN demonstrates much better thermal stability and a significantly higher electronic bandgap[41].

HBN is the most stable form of the three crystalline structures (HBN, cubic BN, and wurtzite BN) and is bonded by strong covalent bonds in a honeycomb configuration while the multiple layers are attached by van der Waals forces, oriented in such a way that B and N atoms are placed above and below each other in adjacent layers [41]. The crystal structure of BN materials are similar to graphene, however, BN demonstrates much better thermal stability and a significantly higher electronic bandgap [41]. Embedding GQDs into

HBN nanosheets has proven to be an effective way to impart stability to the GQDs while maintaining their physicochemical properties [37]. Due to the large bandgap characteristic of HBN, it is entirely non-conductive which can hinder imaging. Introducing GQDs into the lattice of HBN imparts conductivity to the nanoparticle while maintaining chemical and thermal stability.

GQBN: Hexagonal boron nitride-graphene quantum dots

Graphene quantum dot - hexagonal boron nitride (GQBN) nanoparticles are a novel nanomaterial that has only recently been investigated. There are only a few studies to date that exist within the literature, proving that their full potential has yet to be realized. Peng et al., synthesized the nanocomposites to investigate their utility in fluorescent cell imaging and showed that the GQBNs were cell penetrating and biocompatible, and could therefore be used as a promising nanoprobe for intracellular imaging and therapeutics [40]. GQBNs have been used to design electrochemical biosensors for stable, selective, and interference-free neurotransmitter analysis [42]. Researchers have successfully prepared stable sub-10 nm GQD arrays and asserted that HBN embedding promotes physical exploration and potential for large-scale applications [37]. In another study, HBN nanosheets supported GQD composites demonstrated superior microwave absorption performance, a large bandwidth, good thermal conductivity, and excellent chemical and temperature stability [43].

In this study, GQBNs are easily and efficiently synthesized and investigated for their use in bioimaging applications for cancer diagnostics. The nanocomposite synthesis is fast, cheap, reproducible, requires minimal materials, and does not necessitate specialized equipment. There are no studies to date that prioritize a green synthesis

approach for GQBNs. There are also no studies to date that investigate the interactions of GQBNs with cancer cells for Raman imaging. Additionally, GQBNs have not been investigated as SERS nanoparticles. This study will fill these gaps while providing a foundation for a novel approach to cancer detection using quantum-sized biocompatible SERS nanoparticles. To optimize the specificity and selectivity of the GQBNs, targeting moieties can be designed and conjugated to the surface of the nanocomposites. For gynecological cancers, folic acid may be used as a targeting moiety, as many gynecologic cancer cells have folate receptors.

FA-GQBN: Folic acid-conjugated GQBNs

In cancer cells, especially those associated with the female anatomy, the folate receptor (FR) is overexpressed on the cancer cell surface[44]. The overabundance of the folate receptor provides a robust targeting strategy for nanoparticles. Folic acid (FA) binds specifically to these folate receptors while also encouraging endocytosis of the nanoparticle into the cell, therefore conjugating folic acid to the surface of the nanocomposites will allow specific binding to the target cancer cells[44]. There are several studies within the literature that successfully conjugate FA to the surface of GQDs. A 2014 study by Wang et al. used FA-conjugated GQDs loaded with the antitumor drug Doxorubicin (DOX) to target HeLa cells[45]. The DOX-GQD-FA nanoparticles targeted tumor cells differentially and effectively[45]. The nanoparticles allowed real-time monitoring of the cellular uptake and drug release of the nanoassembly while significantly reducing cytotoxicity to non-target cells[45]. This research will be used as a model for attaching FA

to the GQDs within the GQBN nanocomposites. The chemical structure for GQDs, HBN, and folic acid can be viewed in Figure 2.

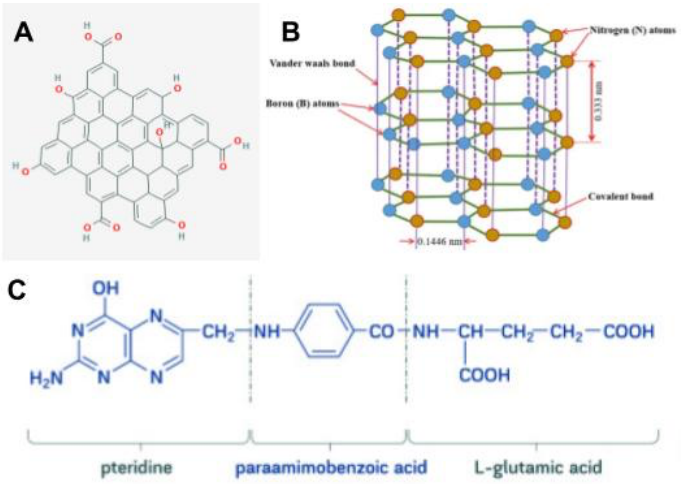

Figure 2. Chemical structure of (A) GQDs, (B) HBN, and (C) folic acid[46–48].

In this study, FA-GQBNs are synthesized using inexpensive, environmentally friendly materials and methods. To synthesize size-controlled, reproducible, high-yield GQDs, organic short grain white rice served as the raw material. Following the nanocomposite synthesis, the GQBNs were conjugated with folic acid to allow specific and selective sensing of FR-positive 4T1 breast cancer cells. These nanomaterials were facilely and efficiently synthesized and investigated for use in bioimaging applications for cancer diagnostics. In the following passages, the synthesis methods and subsequent characterizations for the FA-GQBNs will be reported while detailing the experimental findings and providing plans for future work.

Chapter 2: Scope of Thesis

Hypothesis

GQDs can be efficiently synthesized from organic short grain white rice and incorporated into HBN nanosheets to combine the physicochemical properties of each material. The GQBN nanomaterial will be Raman-active and possess robust optical properties. Finally, FA can be conjugated to the surface of the GQBN nanoparticle to specifically and selectively target the folate receptor present on the surface of breast cancer cells to form a novel SERS platform for cancer cell sensing and probing. The FA-GQBN particles are predicted to perform as robust SERS labels for identifying FR+ cancers *in vitro*. This hypothesis will be tested by the following specific aims:

Aim 1: Optimize the fabrication and characterization of GQDs from organic rice grains.

GQDs will be synthesized from organic short-grain white rice using a bottom-up green synthesis approach. The as-synthesized GQDs should be biocompatible while possessing robust optical properties and a narrow size distribution. They should be a Raman-active, nanoscale material with a hydrodynamic diameter less than 10 nm.

Aim 2: Optimize the fabrication and characterization of GQBN nanocomposites.

GQBN nanocomposites will be prepared through a novel, straight-forward, and biocompatible synthesis approach. The GQBNs should retain the physicochemical properties of GQDs and HBN. They also should be Raman-active, biocompatible, and can be used as SERS tags.

Aim 3: Optimize the fabrication and characterization of FA-GQBN nanocomposites and apply them as SERS labels.

Folic acid will be conjugated to the GQBN nanoparticles. The FA-GQBN nanocomposites should be biocompatible while retaining the robust optical and physicochemical properties of the GQBN particle. The FA-GQBN will then be applied as SERS labels for rapid cancer cell detection.

Chapter 3: Materials and Methods

The HBN nanosheets were purchased commercially from MSE supplies, while the GQDs were prepared through a bottom-up, green synthesis strategy[36]. The use of sustainable, environmentally friendly, and cost-effective materials was prioritized for the nanocomposite synthesis. For the GQDs, the materials used included organic short grain rice purchased from Amazon, deionized (DI) water, and diluted hydrochloric acid purchased from ThermoFisher, adjusted to a pH of ~4 by the addition of DI water. Additional materials for the GQD synthesis included a DmofwHI cordless coffee grinder purchased from Amazon, Phosphate Buffer Solution (PBS) from ThermoFisher, 1.5 mL Eppendorf tubes, 50 mL centrifuge tubes purchased from Sigma Aldrich, 500 mL beakers purchased from Cole-Parmer, 12-14 kDa molecular weight cutoff Spectra/Por 2 dialysis tubing purchased from Repligen, disposable dialysis tubing clamps purchased from Flinn Scientific, 10 mL Luer-Lok tip syringes with 0.22 micrometer filter tips and milliporous membranes from Millipore Sigma, and Steriflip filter units for vacuum filtration from Millipore Sigma. For synthesis, a Heidolph Rotovac Valve Tec vacuum was used for vacuum filtration, a Branson 3800 Ultrasonic Cleaner bath was used for sonication, and a Mettler Toledo Seven Compact pH probe was used to confirm the pH of the dialysis bath. Cell viability assays with the GQDs and GQBNs were carried out using 4T1 breast cancer cells, purchased from ATCC, with an XTT (sodium 3´-[1- (phenylaminocarbonyl)-

3,4- tetrazolium]-bis (4-methoxy6-nitro) benzene sulfonic acid hydrate) Cell Proliferation Assay kit purchased from Sigma Aldrich. Commercial GQDs, which served as controls for the XTT assay, were purchased from ACS Materials. SERS measurements were performed with A549 cells and HEC1A cells purchased from ATCC.

The nanocomposites have been extensively characterized using Fourier transform infrared spectroscopy (FTIR); dynamic light scattering (DLS); ultra-violet visible spectroscopy (UV-Vis); scanning electron microscopy (SEM); energy-dispersive x-ray spectroscopy (EDS); transmission electron microscopy (TEM); and Raman spectroscopy. For FTIR, a Thermo Scientific Nicolet iS-50 with the Attenuated Total Reflection module was utilized with 64 scans and a resolution of 1 cm^{-1} for data collection. To perform FTIR, 20 µL of each sample was pipetted onto the collection stage and left to air dry for one hour. Before analyzing each sample with FTIR, the background is collected and subtracted from the sample spectra to account for environmental fluctuations[49]. FTIR was performed on the GQDs, HBN powder, GQBNs, folic acid, and FA-GQBN in the range of 4000 cm^{-1}-500 cm^{-1}. The data collection and processing software used for FTIR was OMNIC Specta. The FTIR spectra was further analyzed and regenerated using GraphPad Prism. A Renishaw InVia Raman spectrometer, outfitted with both red and green lasers was used for Raman spectroscopy, with WiRE Chememetrics software used for data collection. The red laser, with a wavelength of 785 nm, was used for all Raman measurements with 20 s exposures and 4 accumulations per scan. A Malvern Zetasizer Nano ZS with Zetasizer software was used to carry out DLS, and an Agilent Cary 5000 UV-Vis-NIR Spectrophotometer was used to perform UV-Vis. SEM was performed on a ThermoFisher Quattro S Field Emission Environmental Scanning Electron Microscope

with EDS and ColorSEM and TEM was performed on a JEOL JEM-2010F Field Emission Transmission Electron Microscope. For TEM imaging, a 200 keV accelerating voltage and small spot size were used. To obtain the electron diffraction pattern a distance of 30 cm between sample and detector was used for data collection. Brightness and contrast adjustments were made to the TEM images with the Java-based image processing program ImageJ. To analyze the XTT cell viability assay data, a Student's T-test, one-way ANOVA, and Tukey's Honest Significant Difference (HSD) were performed to determine statistical significance. The protocol for GQD synthesis, HBN preparation, GQBN synthesis, as well as the characterization results will be detailed below.

GQD synthesis

To synthesize the GQDs, 12 grams of rice were weighed and washed to remove residual starches and impurities. The process involved placing the washed rice in disposable perforated weigh boats, then positioning over 500 mL beakers and covering with Parafilm for overnight storage. The dried rice was then ground in bulk in a coffee grinder. The rice powder was then placed in a 500 mL beaker and heated at 200°C under constant stirring conditions for exactly 10 minutes. Rice powder contains a large amount of starch in the form of amylose, an unbranched d-glucose chain, and amylopectin, which has glucose units linked linearly[36]. Upon heating the rice powder, the thermal breakdown of starch leads to glucose oligomers; when the oligomers of glucose are heated to a high temperature of 200°C nucleation takes place and pyrolysis of the glucose molecule leads to the growth of the GQD particle[36]. After heating, the rice powder was placed in a 50 mL centrifuge tube and 25 mL of PBS was added. The solution of rice powder and PBS was

sonicated for an hour in a sonication bath followed by vacuum filtration using a .22 µm SteriFlip vacuum filtration system to obtain a clear solution. This solution was placed in 12-14 kDa MWCO dialysis tubing and submerged in a dialysis bath of HCl, diluted to a pH of 4, for 4 days to remove additional, unreacted starches. After 4 days of dialysis, the GQD solution was obtained and refiltered through a 12 mL syringe with a 0.22 µm Luer-lock tip and placed in 1.5 mL Eppendorf tubes for characterization. The resulting GQDs had a concentration of 2.50 mg/mL, as determined by the gravimetric method. The workflow for the GQD synthesis is depicted in Figure 3.

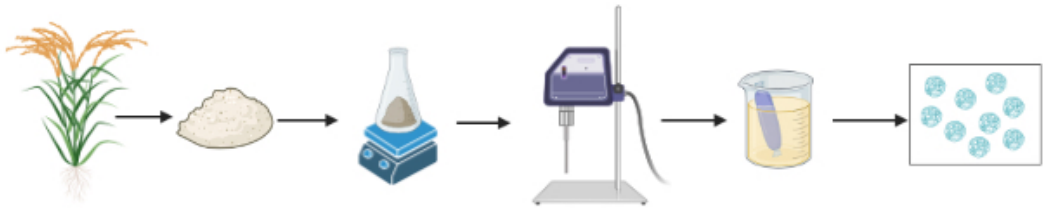

Figure 3. Schematic for green synthesis of GQDs from rice. Briefly, rice is ground into a fine powder, heated at 200°C, sonicated, and then dialyzed for 4 days to obtain a solution of GQDs.

GQBN synthesis

To prepare the HBN for the nanocomposite synthesis, ~11 mg of the HBN powder was added to 5 mL of PBS and then placed in a sonication bath for 45 minutes to make the surface positively charged[40]. Subsequently, 3 mL of the GQD solution was incorporated into the HBN-PBS solution. Next, the HBN and GQDs were combined through electrostatic interactions by tip sonication using an amplitude of 30 Hz. The solution was sonicated in 30 second intervals for 5 minutes to obtain GQBN nanocomposites.

FA-GQBN synthesis

After obtaining the GQBN nanocomposites, FA was conjugated to their surface. To perform the FA-GQD conjugation, the following materials were needed: 96 mg 1-ethyl-3-(3-dimethylaminopropyl)carbodiimide hydrochloride (EDC), purchased from Sigma Aldrich; 11.5 mg N-hydroxysuccinimide (NHS), purchased from Sigma Aldrich; PBS; 10 mM, 1.0 mL folic acid, purchased from ThermoFIsher; 10 mM hydroxylamine, purchased from ThermoFisher; and 1000 Da molecular weight cutoff (MWCO) dialysis tubing. For dialysis, a Pur-A-Lyzer Mega Dialysis Kit, purchased from ThermoFisher, was used. To perform the conjugation, 5 mL of GQD solution was placed in a 100 mL beaker and allowed to react with 96 mg EDC and 11.5 mg NHS in 3 mL of PBS buffer for 30 minutes at room temperature. After 30 minutes, 1.0 mL of 10 mM FA was added to the mixture to obtain a bright yellow solution. The solution was allowed to stir at 200 min^{-1} overnight for approximately 20 hours. After 20 hours, 10 mM of hydroxylamine was added to the solution to quench the reaction. Next, the bright yellow solution was placed in 1 kDa MWCO Mega Dialysis Kit. The dialysis tube was placed in a 500 mL beaker containing 200 mL PBS and dialyzed while stirring the buffer for 27 hours. After 27 hours, the solution within the dialysis tube was clear. The dialysis tube was removed from the PBS buffer and rinsed in DI water before being collected in a 15 mL centrifuge tube for characterization.

Chapter 4: Results and Discussion

GQD, HBN, and GQBN Physicochemical Characterizations

DLS and Zeta Potential Measurements

The physicochemical properties of the GQDs, HBN, and GQBNs were assessed through several different characterization techniques. The photographs of commercial GQDs, synthesized GQDs, commercial GQBN, synthesized GQBN, and HBN powder in Figure 4 depict that all the different GQD solutions were translucent while the HBN powder was an opaque white solution. The nanoparticle size was measured using DLS. Figure 5A shows that the GQDs had an average nanoparticle diameter of 4.1 nm with a 22.2% standard deviation. This is similar to the GQD diameters reported by other green synthesis methods[34,36,50,51]. The synthesized GQDs have a narrow size distribution, proving that the bottom-up, green synthesis from rice was successful. The HBN nanosheets cannot be measured through DLS, however, the manufacturer reported nanoparticle diameters between 100 nm – 200 nm. This was confirmed by conducting measurements on SEM images using ImageJ [52,53]. Figure 5B depicts the nanoparticle diameter for the GQBNs, which showed a normal distribution of diameters between 150 nm- 450 nm. This is larger than what was reported for the diameter of the HBN, which suggests that there are GQDs on the surface, resulting in a larger diameter than what was reported for the HBN alone. Previous GQBN studies did not conduct DLS measurements and therefore do not report nanoparticle diameters.

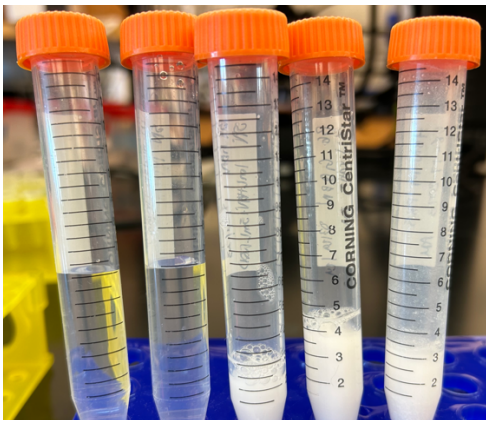

Figure 4. Photograph of (from left to right) commercial GQDs, synthesized GQDs, commercial GQBN, synthesized GQBN, and HBN powder.

Zeta Potential

Figure 5C displays the results for the zeta potential measurements. GQDs have a negative zeta potential of -18 mV. The zeta potential of the HBN before the first sonication step was -25 mV. The zeta potential for the HBN post-sonication was +15 mV, which proves the first sonication step reversed the surface charge of the HBN to allow electrostatic interactions between the HBN and GQDs as was suggested by Peng et al.[40]. Sonication is a common surface modification for HBN that, when performed in an ionic medium, results in oxidation of the molecule, resulting in a reversal of its surface charge[54].

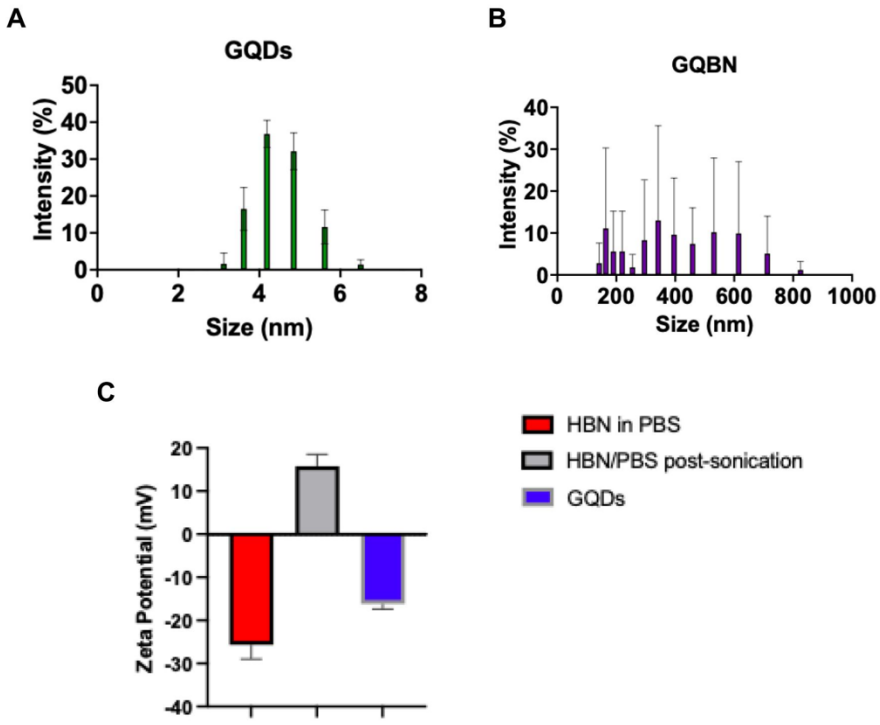

Figure 5. DLS and zeta potential measurements. (A) GQD nanoparticle diameter and size distribution. (B) GQBN nanoparticle diameter and size distribution. Colored bars for 1A and 1B represent measured mean hydrodynamic dimeter, error bars show standard deviation for n = 3 replicates. (C) Zeta Potential measurements. Colored bars in 1C represent measured mean zeta potential values, error bars represent standard deviation for n= 3 replicates.

SEM

SEM images of GQBNs in Figures 6A-C display disc-like structures, which is characteristic of HBN. Figure 6B shows small, dot-like structures characteristic of GQDs surrounding the surface of the HBN discs. When analyzed in ImageJ, the nanoparticle diameters observed in the SEM images agree with the results obtained from DLS. Through x-ray analysis called energy dispersive x-ray spectroscopy (EDS), elemental maps with color overlays were generated. Figures 6C and 6D are the same image, however, 6D shows the color overlay generated by EDS. The green color observed on the HBN surface is attributed to oxygen atoms, while the blue represents carbon atoms. As there is no oxygen or carbon present in HBN, the oxygen and carbon present on the

HBN surface can be attributed only to the presence of GQDs. This confirmed that the GQDs were in fact present on the surface of the HBN, which suggests that their binding was successful. This technique is often used in tandem with SEM or TEM to identify nanoparticles that are too small to be imaged with a traditional SEM[55,56].

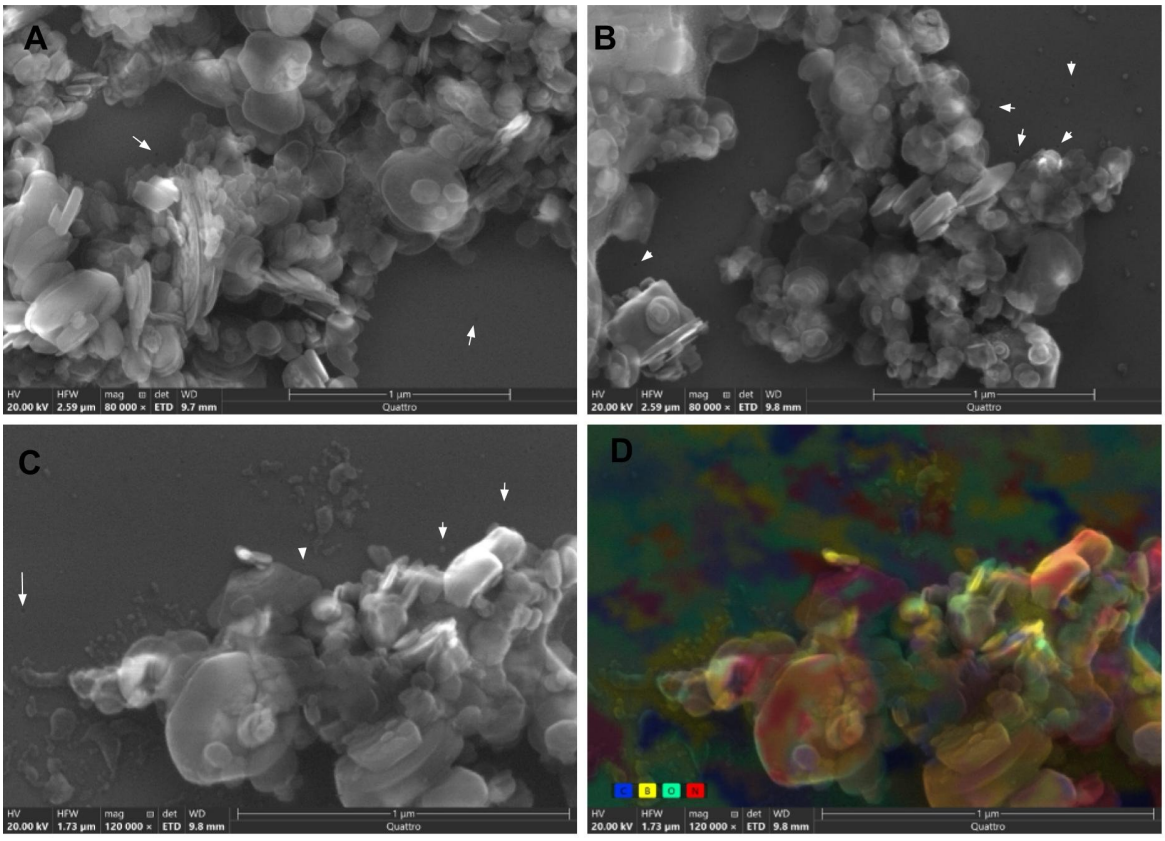

Figure 6. SEM images of GQBNs. (A) Disc-like structures representative of HBN nanosheets. (B) HBN nanosheets with GQDs surrounding the surface, indicated by white arrows. (C) Higher magnification imaging of GQBNs. (D) EDS image obtained from (C) but with ColorSEM; blue and green colors correspond to the GQDs. Scale bar = 1 µm.

TEM

Figure 7 shows TEM images of the GQDs and GQBN nanocomposites. In Figure 7A, the HR-TEM micrograph of the GQDs exhibit several lattice fringes which confirms the GQDs to be a crystalline material. Figure 7B depicts a diffraction pattern of the GQBN particle.

A TEM electron diffraction pattern is a two-dimensional scattering pattern formed when an electron beam interacts with a crystalline sample and reveals information about the atomic arrangement and crystal structure of that material[57]. The elliptical diffraction pattern seen in figure 7B is unique and can be attributed to the interaction of two distinct crystalline lattice types, i.e. the HBN and the GQDs. Figure 7C is a bright-field TEM image of the GQBN nanocomposites, while Figure 7D is the corresponding dark-field TEM micrograph. Bright-field TEM images are formed from the transmitted electron beam, while dark-field images are formed from the electron beam diffracted off the atomic lattices of the crystalline sample[57]. Dark-field imaging in TEM is a technique that selectively enhances contrast from specific crystallographic features within a sample while providing information about the crystallography of the material[57]. The TEM micrographs confirm the synthesized nanocomposites are ordered, crystalline, nanoscale materials.

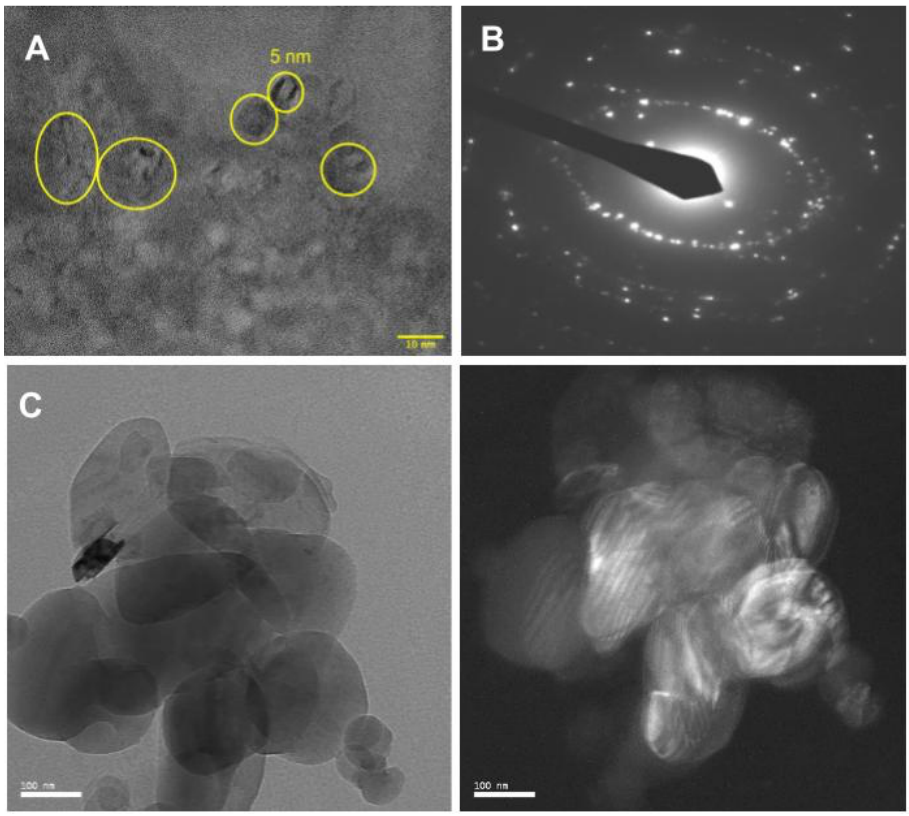

Figure 7. (A) HR-TEM image of GQDs showing lattice fringes. Scale bar = 10 nm. (B) Diffraction pattern of the GQBN particle at 30 cm. (C) Bright-field TEM of GQBN particle. Scale bar = 100 nm. (D) Dark-field TEM of the same GQBN particle. Scale bar = 100 nm.

FTIR

The FTIR results for the GQDs, HBN, and GQBN are displayed in Figure 8. In the spectra for the GQDs in Figure 8A, there was a strong and broad -OH peak observed at 3320 cm^{-1}. There were =C-H stretching vibrations at 2920 cm^{-1} and C-H stretching at 2850 cm^{-1} [58]. The peaks at 1650 cm^{-1} and 1540 cm^{-1} were attributed to C=O bonds[40] and >C=C< bonding[43] respectively. The peak at 1460 cm^{-1} was due to the vibrations in $>CH_2$ groups, while the peaks observed from 1320-1080 were due to C-O bonds[40,58]. In the spectra for the HBN shown in 8B, there were only two peaks at 1330 cm^{-1} and 758 cm^{-1} attributed to -BN bonding and B-N-B bonding, respectively[40,43]. For the GQBN nanocomposites in

Figure 8C, there were several observable peaks that were attributed to both the GQDs and HBN. The peak at 3390 cm^{-1} was due to -OH stretching vibrations from the GQDs[40,58,59]. The peaks at 1700 cm^{-1} and 1360 cm^{-1} were due to B-N bonding, while the peak at 1640 cm^{-1} was due to C=O bonding[43,59,60]. The peak at 1080 cm^{-1} was due to C-O bonding, the peak at 975 cm^{-1} was due to B-N-O bonding, and the peak at 776 cm^{-1} was due to B-N-B bonding[40,59,60]. The new peak at 975 cm^{-1} confirms the bonding of the GQDs with HBN. The presence of new peaks in the GQBN spectra are due to the formation of new bonds between the GQDs and HBN. The very strong peak seen in the GQD spectra at 1650 cm^{-1} is negligible in the spectra for the GQBNs, while the GQD peaks at 1540 cm^{-1} and 1450 cm^{-1} have disappeared. This is due to the rearrangement of bonds in the GQDs and the formation of new bonds with HBN. The GQBN nanocomposites have peaks characteristic of both HBN and GQDs, which further confirms their successful synthesis.

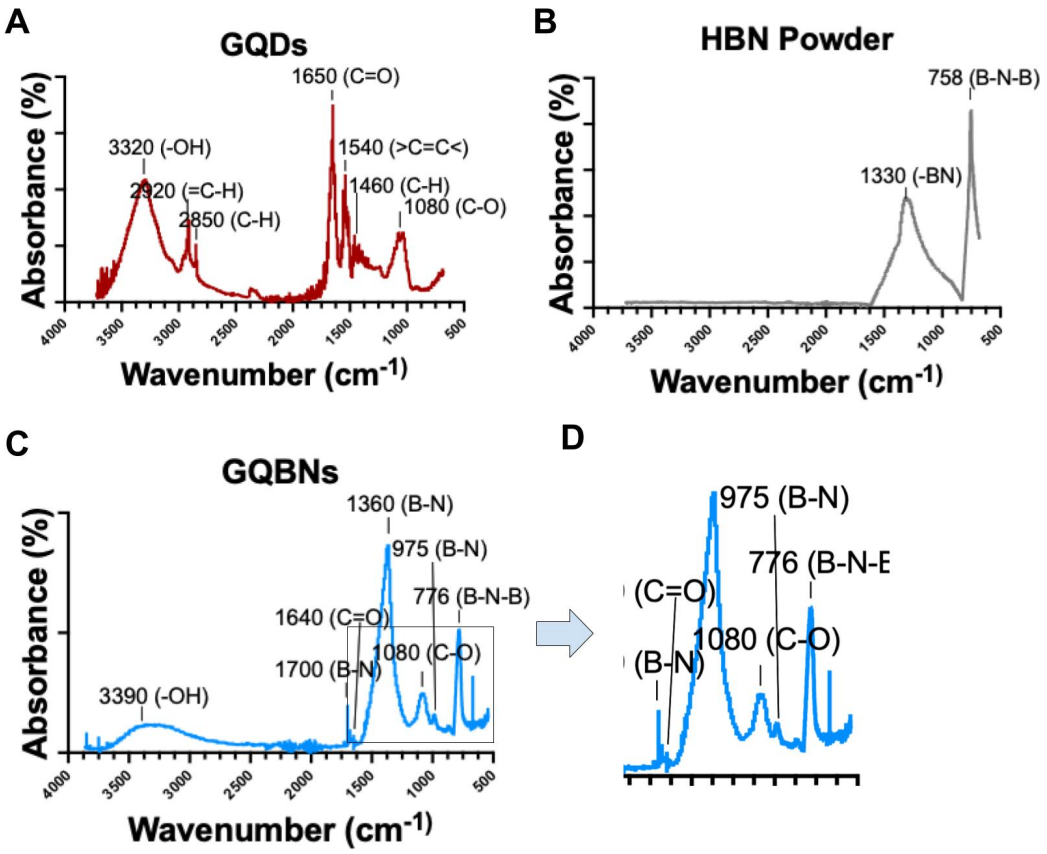

Figure 8. FTIR spectra for GQDs, HBN, and GQBNs. (A) FTIR spectra for GQDs. (B) FTIR spectra for HBN powder. (C) FTIR spectra for GQBN nanocomposites. (D) Zoomed in snapshot of the peak at 975 cm^{-1} from (C).

Raman Spectroscopy

Figure 9 displays the results of Raman spectroscopy performed on the GQDs, HBN, and GQBNs using the red laser with a wavelength of 785 nm. The stronger excitation wavelength was well-tolerated by the nanomaterials, which suggests they are a robust material, as many other nanomaterials are destroyed when irradiated with a strong laser[61]. Figure 9A shows the Raman spectra for the HBN powder, which has one single peak at

1367 cm^{-1} that is attributed to the characteristic E_{2g} signal from in-plane vibrations of boron and nitrogen atoms[62]. This narrow Raman E_{2g} is further evidence of the high quality of the nanomaterial[54]. Figure 9B shows the Raman spectra for the GQDs and Figure 9C shows the Raman spectra for the GQBNs. The GQDs have a characteristic "M" shape to their spectra with peaks at 1350 cm^{-1} and 1640 cm^{-1}, with a sharper peak in between located at 1555 cm^{-1}. The peak observed at 1350 cm^{-1} is referred to as the D-band or disorder peak, while the peaks at 1555 cm^{-1} and 1640 cm^{-1} are referred to as the G-band or graphitic peak[58]. The D-band is present in the GQD spectra due to the breathing modes of sp^2 atoms in rings as well as disorders in the carbon skeleton due to the presence of functional groups[58]. The G-band can be attributed to the bond stretching of all sp^2 atoms[36]. The G peak is always higher than the D peak, while the ratio of D to G peaks is a measure of defect density of the molecules-- the smaller this ratio, the more ordered the material[36]. The ratio observed between peaks is small which indicates the synthesized GQDs have a uniform, ordered, crystal lattice which was further confirmed through TEM. The spectra for the GQBNs retained the "M" shape of the GQDs with an additional, sharp peak at 1365 cm^{-1}, which confirms the successful conjugation of the HBN and GQDs. The Raman spectra for the GQBNs are in agreement with the spectra obtained by Peng et al. and Chen et al.[40,43]. The spectra for the GQBNs appear to be a perfect overlay of the HBN spectra with the GQD spectra, further confirming their successful synthesis.

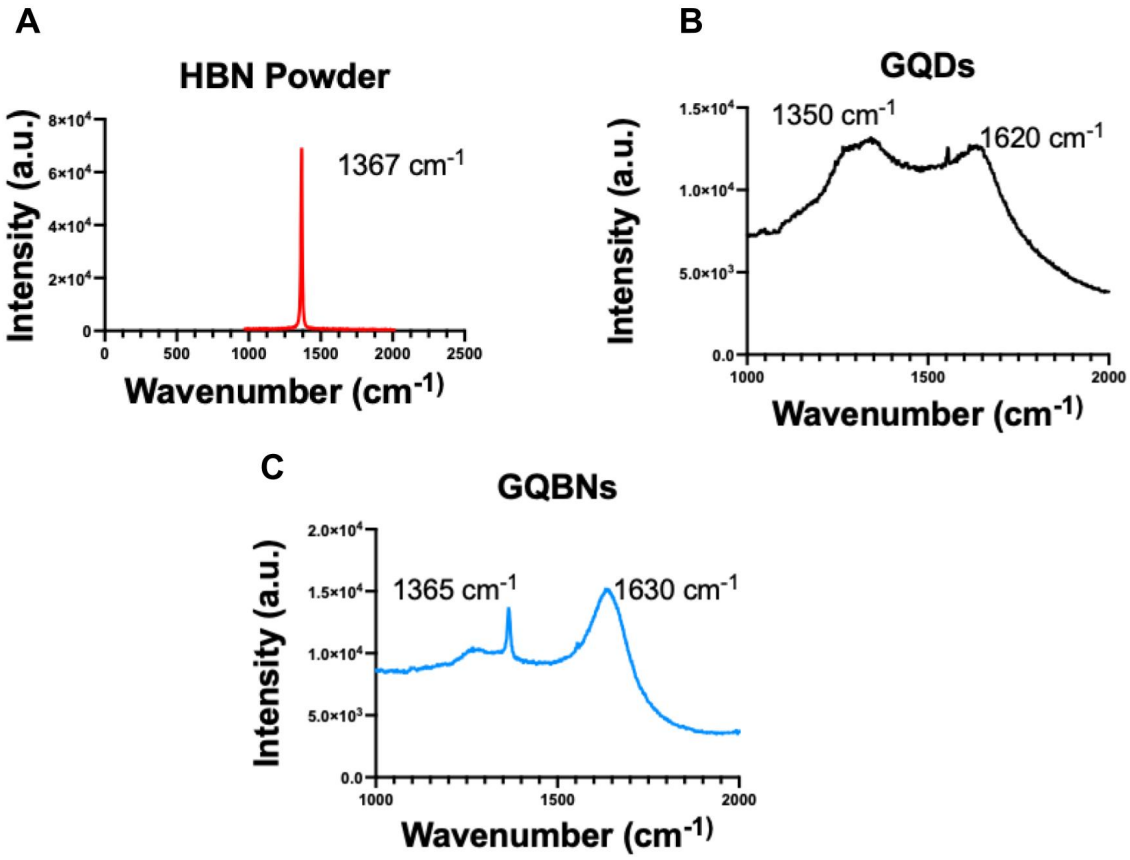

Figure 9. Raman spectra of (A) HBN powder, (B) GQDs and (C) GQBNs.

XTT Biocompatibility Assay

To assess the biocompatibility of the GQBNs, 3-hour and 24-hour XTT assays were performed with 4T1 breast cancer cells. This cell line was chosen as the *in vitro* model due to the abundance of folate receptors present on the cell surface, which will be utilized in future drug delivery studies. The nanoparticle concentration for each group was held constant at 100 μg/mL based on literature and n=6 replicates were used for each

group[36,58,63]. The results for the 3-hour XTT assay can be seen in Figure 10, while the results for the 24-hour XTT assay can be seen in Figure 11. The commercial GQDs and commercial GQBN were used as controls for the synthesized GQBN, HBN, and GQDs. The cell only group in each figure shows 100% cell viability, as this was the positive control group used to normalize the results of the other groups. For the 3-hour XTT assay, both the synthesized GQDs and commercial GQDs performed exceptionally well, with cell viabilities of 136% and 133%, respectively, and standard deviations of 27% and 34%, respectively. These results suggest that the GQDs promoted cell growth. Only one study reports cell proliferative activity of GQDs synthesized from grape seed extract, however, the mechanism is not well-understood, revealing a need for more intensive studies to unravel this potential[58]. A two-tailed t-test was done between the synthesized GQDs and cell only group and determined these results to be significant with a P-value of 0.014, which indicates the synthesized GQDs promoted cell growth. A one-way ANOVA was done for the synthesized GQDs, commercial GQDs, and cell only group and a P-value of 0.0525 was calculated. These differences were not significant, indicating that GQDs do not have a significant effect on cell proliferation. However, they did demonstrate that the GQDs are biocompatible. Following the ANOVA, a Tukey HSD stats was performed and found the following pairs to be significantly different: synthesized GQDs and HBN, commercial GQDS and HBN. The HBN group had a 74% cell viability at 100 µg/mL and a standard deviation of 14%. The synthesized GQBN and commercial GQBN groups had mean cell viabilities of 117% and 104%, respectively, and standard deviations of 34% and 36%, respectively, which suggests the cell proliferative activity of the GQDs ameliorated

the cytotoxic effects of the HBN. The synthesized nanoparticles were thusly proven to be biocompatible over 3 hours.

The 24-hour XTT assay showed the synthesized GQDs group had a mean cell viability of 125% with a standard deviation of 24% and synthesized GQBN had a cell viability of 130% and standard deviation of 11%, while the commercial GQDs and commercial GQBN had a mean cell viability of 104% and 53% respectively, and standard deviations of 16% and 9%, respectively. After 24 hours the HBN group had a mean cell viability of 102% and standard deviation of 3%. A two-tailed t-test between the synthesized GQDs and cell only group as well as the synthesized GQBN and cell only group showed that these results were statistically significant. A one-way ANOVA between the synthesized GQDs, commercial GQDs, and cell only group showed these results were also significant, as did the one-way ANOVA between the cell only group, synthesized GQBN, and commercial GQBN groups. After ANOVA, Tukey's HSD test showed significant differences between the means of these pairs: cell only vs. synthesized GQBN, cell only vs. commercial GQBN, synthesized GQDs vs. commercial GQBN, commercial GQDs vs. commercial GQBN, synthesized GQBN vs. commercial GQBN, synthesized GQBN vs. HBN, and commercial GQBN vs. HBN. These results suggest that the synthesized nanoparticles performed better than the commercial nanoparticles. The as-synthesized nanoparticles were not only biocompatible, but also demonstrated cell proliferative activity. Any cytotoxic effects that result from the presence of HBN are ameliorated by the cell proliferative activity of the GQDs. The cell proliferative activity of the GQDs indicates the occurrence of epigenetic modifications within the genome of the cell. Numerous research groups have observed this phenomenon, including Kumawat et

al. and Ahina et al., however, none have uncovered a definitive cause for this occurrence[58,64].

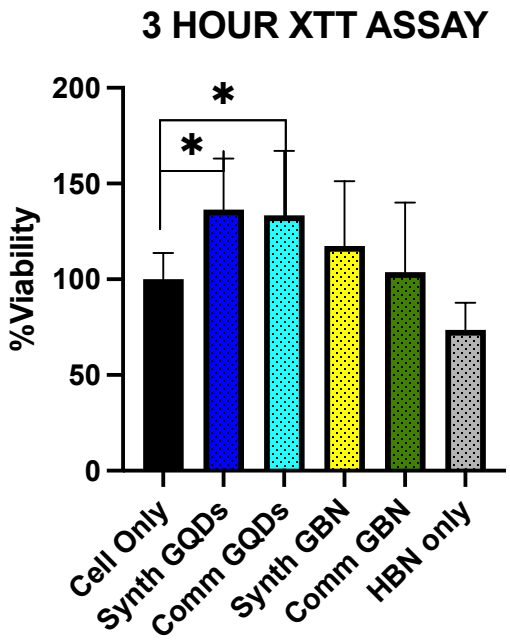

Figure 10. 3-hour XTT cell viability assay results. Colored bars represent the measured mean cell viability normalized to the cell only group. Error bars represent the standard deviation for n = 6 replicates, asterisks denote significance. Asterisk (*) denotes significance based on two-tailed t-test.

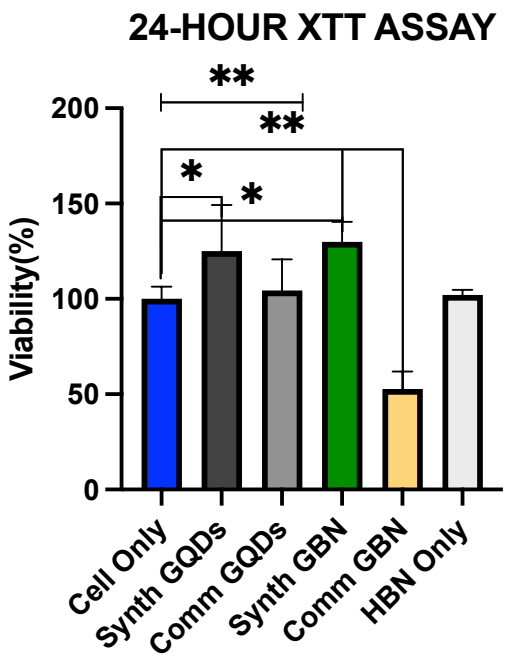

Figure 11. 24-hour XTT assay results. Colored bars represent the measured mean cell viability normalized to the cell only group. Error bars represent the standard deviation for n = 6 replicates, asterisks denote significance. Single asterisk (*) denotes significance based on two-tailed t-test. Double asterisk (**) denotes significance based on one-way ANOVA.

Table 1. 3-hour XTT Cell Viability Percent Increases.

Group	Cell Viability	Std. Dev.	Cell viability % increase
Cell Only	100%	14%	N/A
Synthesized GQDs	136%	27%	+36%
Commercial GQDs	133%	34%	+33%
GQBN with Synth GQDs	117%	34%	+17%
GQBN with Comm GQDs	104%	36%	+4%
HBN only	74%	14%	-26%

Table 2. 24-hour XTT Cell Viability Percent Increases.

Group	Cell Viability	Std. Dev.	Cell viability % increase
Cell Only	100%	6%	N/A
Synthesized GQDs	125%	24%	+25%
Commercial GQDs	104%	16%	+4%
GQBN with Synth GQDs	130%	11%	+30%
GQBN with Comm GQDs	53%	9%	-47%
HBN only	102%	3%	+2%

Folic Acid and FA-GQBN Physicochemical Characterizations

DLS

DLS was used to measure the diameter of the folic acid and FA-GQBN nanoparticles. These results can be viewed in Figure 12. The diameter of folic acid in PBS was measured and found to be between 1000 nm- 3000 nm, with an average of 700 nm, seen in Figure 12A. The GQBN nanocomposites had a size range between 200 nm and 400 nm, with the greatest intensity at 400 nm. These results are depicted in Figure 12B. The FA-GQBNs, seen in Figure 12C, were measured and found to be between 500 nm and 1300 nm, with an average of 800 nm. The larger, normally distributed diameter of the FA-GQBN suggests that the folic acid was successfully conjugated to the surface of the nanoparticles.

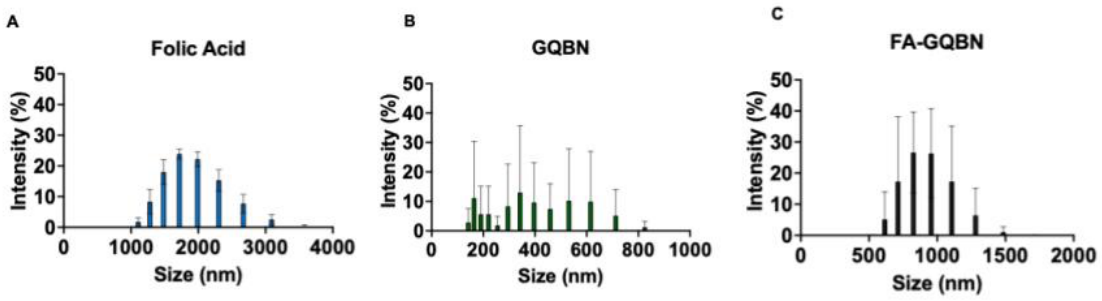

Figure 12. Nanoparticle diameters of (A) Folic acid in PBS, (B) GQBN nanocomposites, and (C) FA-GQBNs. Colored bars represent measured mean hydrodynamic dimeter, error bars show standard deviation for n = 3 replicates

SEM

SEM imaging was performed on the FA-GQBN particles. The same instrument and imaging parameters used for the GQD and GQBN particles were utilized for the FA-GQBN particle. Figure 13 depicts the imaging results. In Figure 13A, a large FA-GQBN particle is observed. The disc-like structures characteristic of HBN can be seen on the particle, with round structures, characteristic of GQDs, on and around the surface. There are additional structures on the particle that could be attributed to the folic acid. EDS with ColorSEM was performed on the particle shown in 13A. The EDS and ColorSEM results are shown in 13B. The yellow and purple colors are attributed to the oxygen and carbon present in the GQDs. While the GQDs are difficult to resolve, the presence of these colors as well as the nanoscale of the structures indicate they are in the solution and present on the FA-GQBN particle. The orange and green colors as well as the shape of the structures indicate the presence of boron and nitrogen, respectively, that are attributed to the HBN. Folic acid also has an abundance of carbon, hydrogen, nitrogen, and oxygen, therefore these images alone do not confirm the synthesis of the particle, however, based on the

other physicochemical characterizations the synthesis was successful. Figure 13C depicts another FA-GQBN particle in solution. Figure 13D is the same particle at a higher magnification. The FA-GQBN particle in 13C and 13D appear asymmetrical but similar in quality to the particle in 13A and 13B.

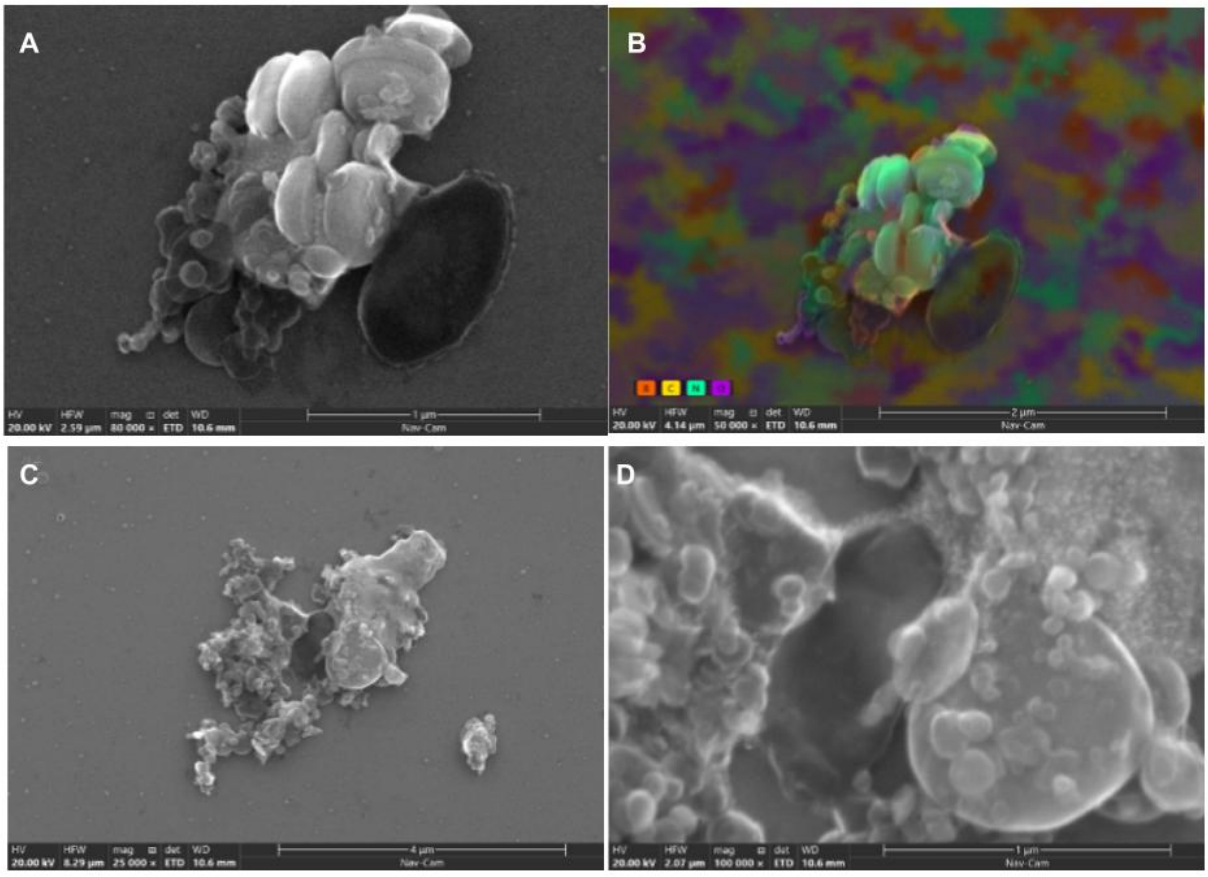

Figure 13. SEM imaging of the FA-GQBN particle. (A) FA-GQBN particle in solution and (B) EDS of (A) with ColorSEM overlay. Scale bar = 1 µm and 2 µm respectively. (C) SEM of a different FA-GQBN particle in solution, and (D) Zoomed in image of particle from (C). Scale bar = 4 µm and 1 µm, respectively.

FTIR

The FTIR results for folic acid in PBS and the FA-GQBN particles are displayed in Figure 14. Folic acid has several characteristic peaks in its IR spectra, seen in 13A. The peak at 3300 cm^{-1} is attributed to the (-OH) groups of folic acid in the crystalline structure[65]. The

peak at 1690 cm^{-1} is attributed to the (-C=O) group present in the pterin structure of folic acid, while the peak at 1610 cm^{-1} is attributed to the bending of (-$CONH_2$) groups[65]. Figure 14B displays the IR spectra for the FA-GQBN particle, where characteristic peaks corresponding to the GQDs, HBN, and folic acid are observed. The broad peak at 3340 cm^{-1} can be attributed to the (-OH) groups present in the GQDs[58]. The sharp peaks at 1360 cm^{-1} and 772 cm^{-1} are due to the boron-nitride bonds present in the HBN[40,43]. The small but distinct peak at 1700 cm^{-1} is due to the formation of an amide bond, attributed to the binding of folic acid with the GQBN particle[66]. The peaks at 520 cm^{-1} and 403 cm^{-1} are due to vibrations involving heavy carboxylate molecular groups and the aromatic ring, respectively, in folic acid[65,67].

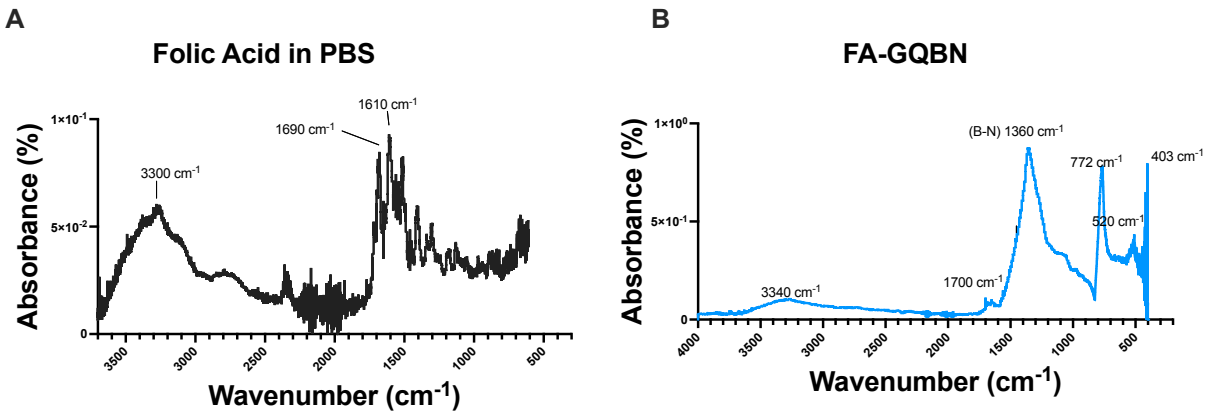

Figure 14. FTIR spectra of (A) Folic acid in PBS and (B) FA-GQBN particle.

Raman Spectroscopy

The Raman spectra for folic acid in PBS and the FA-GQBN particle are depicted in Figure 15. Figure 15A shows the Raman spectra for folic acid in PBS. The intense peak at 1631 cm^{-1} is due to the stretching vibration of NH in the pteridine ring of the folic acid, while the peak at 1255 cm^{-1} is due to the rocking vibration of the C=N from the pteridine[68]. The

Raman spectra for the FA-GQBN particle is displayed in Figure 15B. The characteristic peaks for HBN, GQDs, and folic acid are all present in this spectrum. The peak at 1249 cm^{-1} represents the rocking vibration of the C=N in pteridine of the folic acid, while the peaks at 1350 cm^{-1} and 1628 cm^{-1} represent the GQD peaks. The GQD peak at 1350 cm^{-1} is obscured by the strong peak at 1255 cm^{-1}. The peak for HBN is indistinguishable due to the distinct peaks formed by the GQDs and folic acid. The FA-GQBN spectra retains the characteristic "M" shape of the GQDs and GQBN. This confirms the successful synthesis of the nanocomposite while retaining the optical properties of its constituents.

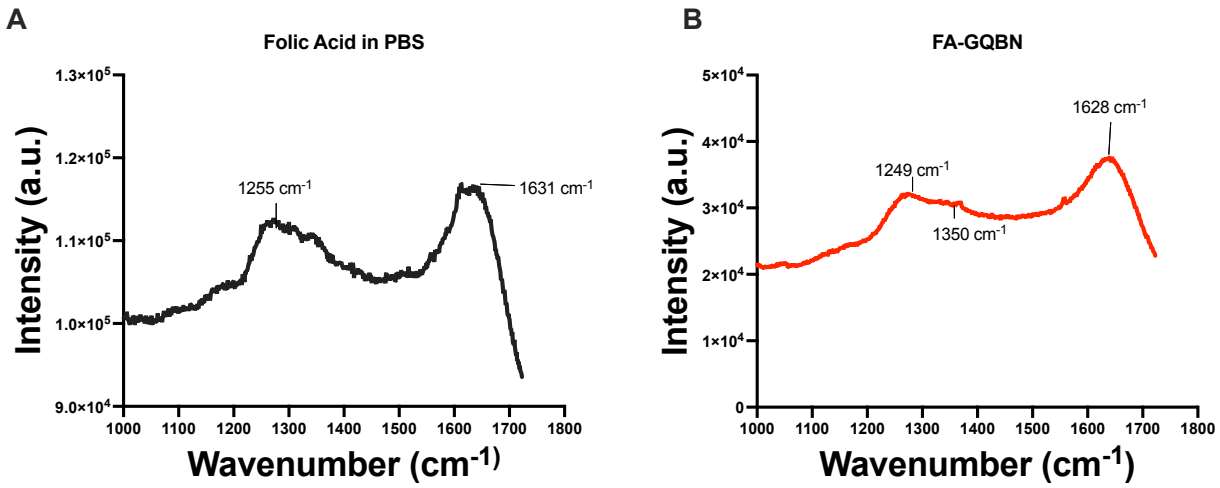

Figure 15. Raman spectra for (A) folic acid in PBS and (B) FA-GQBNs.

XTT Biocompatibility Assay

An XTT biocompatibility assay was performed with the FA-GQBN particle. 4T1 breast cancer cells served as the *in vitro* model. FA-GQBN nanoparticles were added in the concentration of 100 µg/mL. Two nanoparticle incubation times were assessed. A 3-hour assay, shown in 16A, and a 24-hour assay, shown in 16B, were performed with six

replicates for each condition. The cell only group served as the positive control. The results were normalized to the cell only group. For the 3-hour assay the cell only group had 100% cell viability with a standard deviation of 33%. The experimental group had a mean cell viability of 91% with a standard deviation of 17%. For the 24-hour assay, the cell only group had 100% cell viability with a standard deviation of 5%. The experimental group had a mean cell viability of 93% with a standard deviation of 24%. Based on these results it was determined the addition of folic acid to the GQBN particle did not affect its biocompatibility. The FA-GQBN particle is not cytotoxic at this concentration.

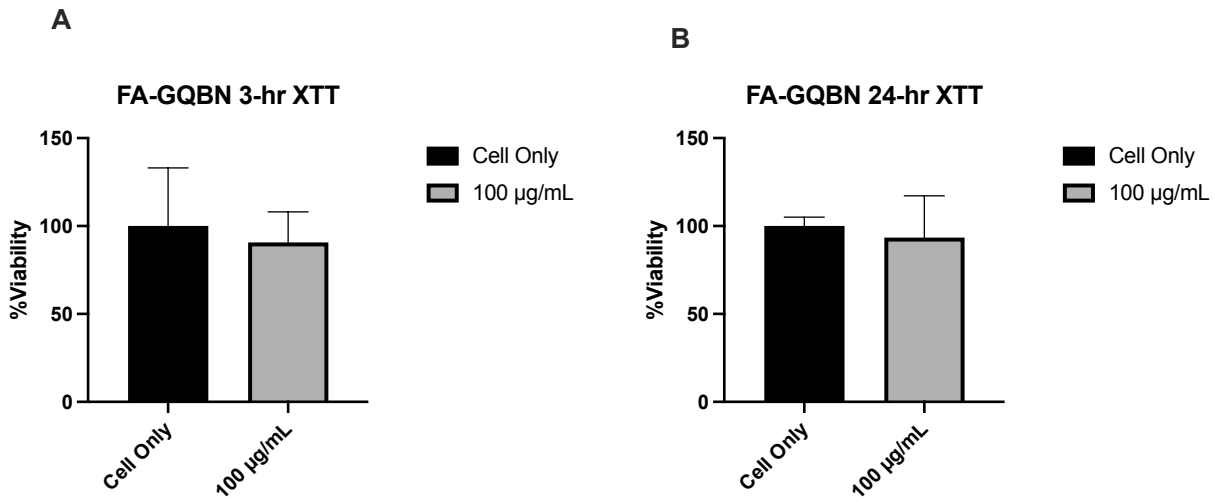

Figure 16. XTT cell viability assay results. (A) 3-hour XTT results and (B) 24-hour XTT assay results. 24-hour XTT assay results. Black and gray bars represent the measured mean cell viability normalized to the cell only group. Error bars represent the standard deviation for n = 6 replicates.

SERS of FR+ and FR- Cancer Cells

Raman spectroscopy was performed with the GQDs and FA-GQBN particles to assess their efficacy as SERS nanoparticles and determine the targeting capacity of the folic acid present on the material. A549 cells lung carcinoma cells served as the FR negative (FR-)

cell line[69]. This was the negative control, as lung cancer cells do not express the folate receptor on their cell membrane[70]. HEC1A endometrial carcinoma cells served as the positive control, as these cells possess an abundance of folate receptors on their cell membrane[71]. Each nanoparticle group was cultured with the respective cell lines with a concentration of 100 μg/mL for 4 hours, followed by chemical fixation with paraformaldehyde. SERS spectra was collected using the same parameters as all previous Raman experiments. Briefly, the 785 nm red laser was used at 100% laser intensity in twenty-second intervals and four accumulations. Figure 17 displays the results obtained from the SERS measurements. In Figure 17A-C the addition of both the GQDs and FA-GQBNs had negligible effects on the spectra for the A549 cells, as only one single prominent peak at 1360 cm^{-1} can be observed in the spectra. This peak is associated with the symmetric stretching of CH_3 in lipids within the cell[20,71]. There are no other discernable peaks in the A549 Raman spectra. This aligns with the expected results. The FA-GQBN nanoparticles did not specifically or selectively interact with the FR- cells and therefore provided very little SERS signal enhancement. The Raman spectra for the FR+ HEC1A cells are shown in Figure 17D-F. In 17D, the spectra for the cell only group has only one prominent peak at 1365 cm^{-1}, attributed to the symmetric stretching of CH_3 in the lipids of the cell[20,71]. In 17E the HEC1A cells were cultured with the GQDs. Due to the nanometer-scale size of the GQDs they were non-specifically uptaken by the cells. The LSPR characteristic of GQDs provided significant SERS signal enhancement. Several new peaks are discernible within the spectrum. The peak observed at 1044 cm^{-1} is attributed to phenylalanine within the proteins of the cell while the peak at 1093 cm^{-1} is due to the nucleic acids present in the cell nucleus of the cell[72,73].The peaks observed at

1232 cm^{-1} and 1294 cm^{-1} are due to the presence of Amide III within the proteins of the cell[72–74]. The small peak at 1345 cm^{-1} can be attributed to the C-H deformation of proteins within the cell[75]. The prominent peak at 1411 cm^{-1} is due to the presence of lipids within the cell[20,74]. Figure 17F depicts the data for the FA-GQBN and HEC1A group. There was no observed SERS signal enhancement provided by the FA-GQBN particle. This could be attributed to several factors concerning the size of the nanoparticles. The micron-sized diameter of the FA-GQBN particle prohibits them from being uptaken by the cells[76]. Additionally, several studies within literature suggest the optimal nanoparticle size for SERS enhancement to be between 30 nm to 100 nm[77–79]. The FA-GQBN particles significantly exceed this parameter. Another major reason for the absence of SERS signal enhancement is related to the LSPR of the FA-GQBN particle. Literature states when the particle size approaches that of the magnitude of the excitation wavelength the particles become preferentially excited in non-radiative modes, which significantly diminishes the SERS effect[77]. The FA-GQBN particles are between 500 nm and 1500 nm, which approaches the scale of the 785 nm laser.

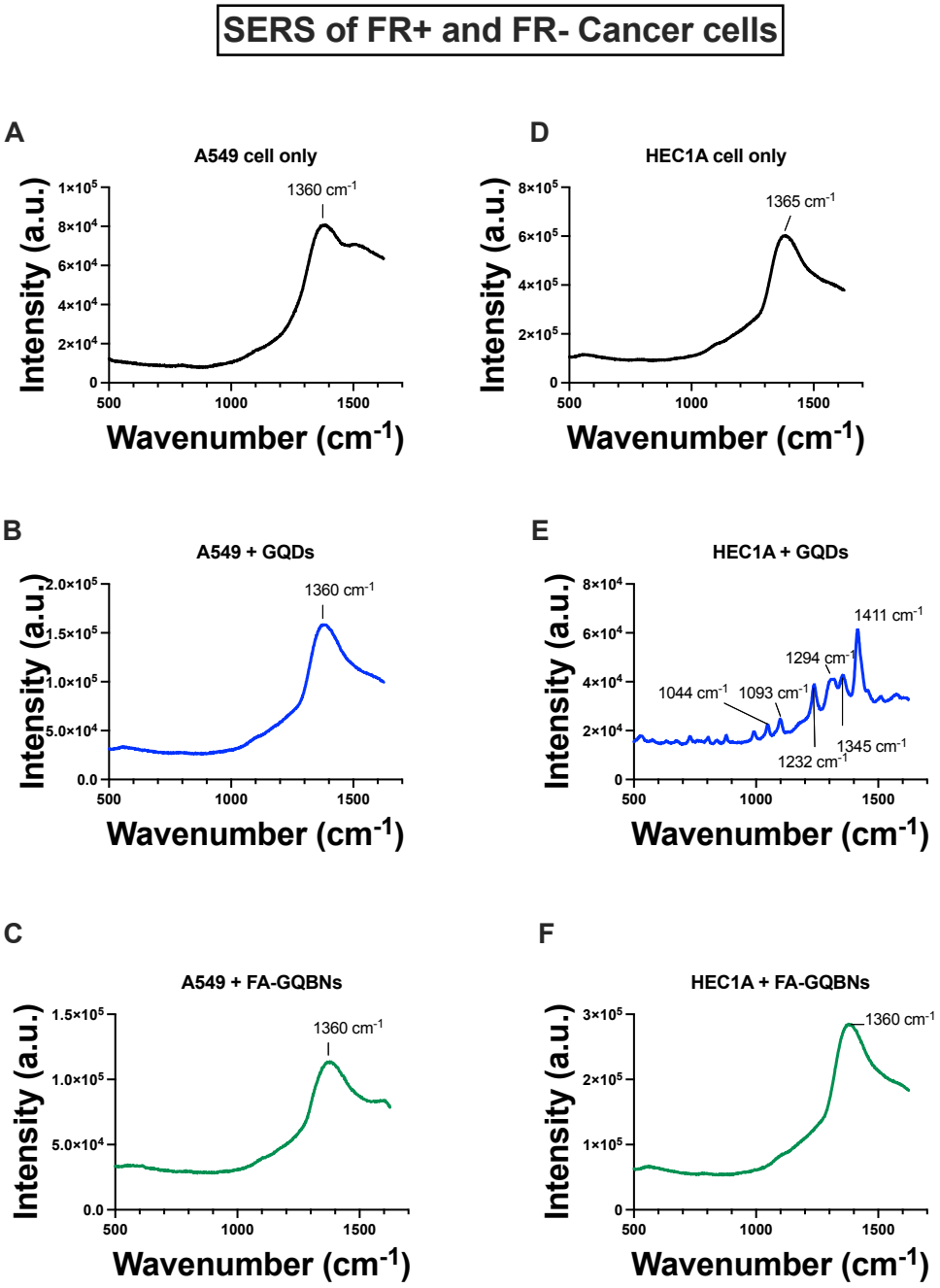

Figure 17. Surface enhanced Raman spectroscopy of FR- and FR+ cancer cells. (A) Spectrum for A549 cells only. (B) Raman spectrum for A549 cells incubated with GQDs. (C) Raman spectrum for A549 cells incubated with FA-GQBNs. (D) Raman spectrum for HEC1A cells only. (E) Raman spectrum for HEC1A cells incubated with GQDs. (F) Raman spectrum for HEC1A cells incubated with FA-GQBN particles.

Chapter 5: Conclusions

The field of nanomedicine is rapidly expanding which reveals the need for a multitude of nanoscale materials for biomedical applications. FA-GQBNs are a novel material with exciting implications for nanomedicine. Individually, both HBN and GQDs have incredible optical, chemical, and physical properties that, when combined, could provide an exciting avenue for improving cancer imaging and diagnostics. GQBNs have only recently been investigated for their use in biological applications, revealing an urgent need to elucidate their properties. In this work, GQBNs followed by FA-GQBNs were successfully synthesized using eco-friendly bio renewable resources and their properties investigated through extensive characterization, with their efficacy as SERS tags also assessed. The GQBN and FA-GQBN synthesis was novel, inexpensive, rapid, straight-forward, and did not require the use of harmful, toxic materials or specialized equipment. The synthesized nanocomposites possessed exceptional physicochemical properties and excellent biocompatibility, which suggests they are an excellent material for biological applications. Application of GQDs for SERS successfully revealed important information about the protein structure of HEC1A cells. Although, conjugating folic acid to the GQDs did not achieve the desired SERS enhancement for cancer cell detection, it offers valuable information for further optimization. The data derived from this research provides new knowledge for SERS platform fabrication by combining the unique properties of HBN and GQD nanoparticles. This research lays the groundwork for future developments in drug delivery systems, nanotherapeutics, and SERS nanoparticles. The versatility of these nanocomposites allows for customization to suit nearly any application, limited only by

the creativity of the researcher. Further development and work with the FA-GQBNs is expected to revolutionize the field of oncological nanotherapeutics.

Future Directions

Based on the findings in this research, the nanoparticles were found to be suitable for their use in biological research. More work needs to be done to improve the overall quality and performance of the nanoparticles. Decreasing the particle size and improving monodispersity while enhancing the colloidal stability of the particles would significantly improve their performance. Work is underway to investigate the use of these particles for *in vivo* applications. The FA-GQBNs will be explored as nanoparticles for photothermal therapy (PTT). GQDs have been exploited as photosensitizers in PTT and show promise in this application. The FA-GQBNs are expected to further improve their efficacy as photosensitizer agents. Additionally, research is underway to load these nanoparticles with drugs and explore their use as drug delivery vehicles.

Bibliography

1. Guerrini, L., Pazos-Perez, N., Garcia-Rico, E. & Alvarez-Puebla, R. Cancer characterization and diagnosis with SERS-encoded particles. *Cancer Nano* **8**, 5 (2017).
2. Sutton, M. Y., Anachebe, N. F., Lee, R. & Skanes, H. Racial and Ethnic Disparities in Reproductive Health Services and Outcomes, 2020. *Obstetrics & Gynecology* **137**, 225 (2021).
3. Armstrong, A. & Maddox, Y. T. Health Disparities and Women's Reproductive Health. *Ethnicity & Disease* **17**, 4–7 (2007).
4. Hall, K. S., Dalton, V. & Johnson, T. R. B. Social disparities in women's health service use in the United States: a population-based analysis. *Annals of Epidemiology* **24**, 135–143 (2014).
5. Eltoukhi, H. M., Vance, A., Troutman, M. & Al-hendy, A. Reproductive Health Care Disparities: Insights and Opportunities. *Current Women's Health Reviews* **14**, 261–266 (2018).
6. Ruiyi, L., Tinling, P., Hongxia, C., Jinsong, S. & Zaijun, L. Electrochemical detection of cancer cells in human blood using folic acid and glutamic acid-functionalized graphene quantum dot-palladium@gold as redox probe with excellent electrocatalytic activity and target recognition. *Sensors and Actuators B: Chemical* **309**, 127709 (2020).
7. Oseledchyk, A., Andreou, C., Wall, M. A. & Kircher, M. F. Folate-Targeted Surface-Enhanced Resonance Raman Scattering Nanoprobe Ratiometry for Detection of Microscopic Ovarian Cancer. *ACS Nano* **11**, 1488–1497 (2017).

8. Verdin, A., Malherbe, C. & Eppe, G. Spatially resolved determination of the abundance of the HER2 marker in microscopic breast tumors using targeted SERS imaging. *Microchim Acta* **188**, 288 (2021).
9. Raman, C. V. & Krishnan, K. S. A New Type of Secondary Radiation. *Nature* **121**, 501–502 (1928).
10. Huang, X., El-Sayed, I. H., Qian, W. & El-Sayed, M. A. Cancer Cells Assemble and Align Gold Nanorods Conjugated to Antibodies to Produce Highly Enhanced, Sharp, and Polarized Surface Raman Spectra: A Potential Cancer Diagnostic Marker. *Nano Lett.* **7**, 1591–1597 (2007).
11. Ikeda, K., Suzuki, S. & Uosaki, K. Crystal Face Dependent Chemical Effects in Surface-Enhanced Raman Scattering at Atomically Defined Gold Facets. *Nano Lett.* **11**, 1716–1722 (2011).
12. Li, J. F. *et al.* Shell-isolated nanoparticle-enhanced Raman spectroscopy. *Nature* **464**, 392–395 (2010).
13. Lv, R. *et al.* Large-Area Si-Doped Graphene: Controllable Synthesis and Enhanced Molecular Sensing. *Adv. Mater.* **26**, 7593–7599 (2014).
14. Muehlethaler, C. *et al.* Ultrahigh Raman Enhancement on Monolayer MoS_2. *ACS Photonics* **3**, 1164–1169 (2016).
15. Nie, S. & Emory, S. R. Probing Single Molecules and Single Nanoparticles by Surface-Enhanced Raman Scattering. *Science* **275**, 1102–1106 (1997).
16. Zhu, Z. *et al.* Superstructures and SERS Properties of Gold Nanocrystals with Different Shapes. *Angew. Chem. Int. Ed.* **50**, 1593–1596 (2011).

17. Wang, J., Liang, D., Jin, Q., Feng, J. & Tang, X. Bioorthogonal SERS Nanotags as a Precision Theranostic Platform for *in Vivo* SERS Imaging and Cancer Photothermal Therapy. *Bioconjugate Chem.* **31**, 182–193 (2020).
18. Choi, N. *et al.* SERS biosensors for ultrasensitive detection of multiple biomarkers expressed in cancer cells. *Biosensors and Bioelectronics* **164**, 112326 (2020).
19. Verdin, A., Malherbe, C., Müller, W. H., Bertrand, V. & Eppe, G. Multiplex micro-SERS imaging of cancer-related markers in cells and tissues using poly(allylamine)-coated Au@Ag nanoprobes. *Anal Bioanal Chem* **412**, 7739–7755 (2020).
20. Haldavnekar, R., Venkatakrishnan, K. & Tan, B. Non plasmonic semiconductor quantum SERS probe as a pathway for in vitro cancer detection. *Nat Commun* **9**, 3065 (2018).
21. Carmicheal, J. *et al.* Label-free characterization of exosome via surface enhanced Raman spectroscopy for the early detection of pancreatic cancer. *Nanomedicine: Nanotechnology, Biology and Medicine* **16**, 88–96 (2019).
22. Chen, H. *et al.* Identification and characterization of bladder cancer by low-resolution fiber-optic Raman spectroscopy. *J. Biophotonics* **11**, e201800016 (2018).
23. Desroches, J. *et al.* A new method using Raman spectroscopy for in vivo targeted brain cancer tissue biopsy. *Sci Rep* **8**, 1792 (2018).
24. Ghaffarkhah, A. *et al.* Synthesis, Applications, and Prospects of Graphene Quantum Dots: A Comprehensive Review. *Small* **18**, 2102683 (2022).
25. Perini, G., Palmieri, V., Ciasca, G., De Spirito, M. & Papi, M. Unravelling the Potential of Graphene Quantum Dots in Biomedicine and Neuroscience. *IJMS* **21**, 3712 (2020).

26. Zmejkoski, D. Z. *et al.* Antibacterial composite hydrogels of graphene quantum dots and bacterial cellulose accelerate wound healing. *J Biomed Mater Res B Appl Biomater* **110**, 1796–1805 (2022).
27. Kumar, Y. R., Deshmukh, K., Sadasivuni, K. K. & Pasha, S. K. K. Graphene quantum dot based materials for sensing, bio-imaging and energy storage applications: a review. *RSC Adv.* **10**, 23861–23898 (2020).
28. Ji, G., Tian, J., Xing, F. & Feng, Y. Optical Biosensor Based on Graphene and Its Derivatives for Detecting Biomolecules. *International Journal of Molecular Sciences* **23**, 10838 (2022).
29. Sundarabharathi, L., Parangusan, H., Ponnamma, D., Al-Maadeed, M. A. A. & Chinnaswamy, M. In-vitro biocompatibility, bioactivity and photoluminescence properties of Eu3+/Sr2+ dual-doped nano-hydroxyapatite for biomedical applications. *Journal of Biomedical Materials Research Part B: Applied Biomaterials* **106**, 2191–2201 (2018).
30. Younis, M. R., He, G., Lin, J. & Huang, P. Recent Advances on Graphene Quantum Dots for Bioimaging Applications. *Front. Chem.* **8**, 424 (2020).
31. Mousavi, S. M. *et al.* Recent Advances in Inflammatory Diagnosis with Graphene Quantum Dots Enhanced SERS Detection. *Biosensors* **12**, 461 (2022).
32. Nelson, S. & Rouf, T. B. Application of SERS Nanoparticles for Imaging for Fast, Sensitive and Selective Cancer Screening: A Review. *SBB* **6**, 595–609 (2023).
33. Panyathip, R. *et al.* Surface Enhanced Raman Scattering in Graphene Quantum Dots Grown via Electrochemical Process. *Molecules* **26**, 5484 (2021).

34. Abbas, A., Tabish, T. A., Bull, S. J., Lim, T. M. & Phan, A. N. High yield synthesis of graphene quantum dots from biomass waste as a highly selective probe for Fe3+ sensing. *Sci Rep* **10**, 21262 (2020).
35. Wang, L. *et al.* Facile synthesis of fluorescent graphene quantum dots from coffee grounds for bioimaging and sensing. *Chemical Engineering Journal* **300**, 75–82 (2016).
36. Kalita, H. *et al.* Efficient synthesis of rice based graphene quantum dots and their fluorescent properties. *RSC Adv.* **6**, 23518–23524 (2016).
37. Chen, D. *et al.* Sub-10 nm stable graphene quantum dots embedded in hexagonal boron nitride. *Nanoscale* **11**, 4226–4230 (2019).
38. Satawara, A. M., Shaikh, G. A., Gupta, S. K. & Gajjar, P. N. Structural, electronic and optical properties of hexagonal boron-nitride (h-BN) monolayer: An Ab-initio study. *Materials Today: Proceedings* **47**, 529–532 (2021).
39. Unal, S. *et al.* Synthesis, characterization, and biological properties of composites of hydroxyapatite and hexagonal boron nitride. *Journal of Biomedical Materials Research Part B: Applied Biomaterials* **106**, 2384–2392 (2018).
40. Peng, J. *et al.* Fabrication of Graphene Quantum Dots and Hexagonal Boron Nitride Nanocomposites for Fluorescent Cell Imaging. *Journal of Biomedical Nanotechnology* **9**, 1679–1685 (2013).
41. Rasul, M. G., Kiziltas, A., Arfaei, B. & Shahbazian-Yassar, R. 2D boron nitride nanosheets for polymer composite materials. *npj 2D Mater Appl* **5**, 1–18 (2021).

42. Yola, M. L. & Atar, N. A novel detection approach for serotonin by graphene quantum dots/two-dimensional (2D) hexagonal boron nitride nanosheets with molecularly imprinted polymer. *Applied Surface Science* **458**, 648–655 (2018).
43. Hu, Q. *et al.* Controllable synthesis and enhanced microwave absorption properities of novel lightweight graphene quantum dots/hexagonal boron nitride composites. *Carbon* **182**, 134–143 (2021).
44. Bittleman, K. R., Dong, S., Roman, M. & Lee, Y. W. Folic Acid-Conjugated Cellulose Nanocrystals Show High Folate-Receptor Binding Affinity and Uptake by KB and Breast Cancer Cells. *ACS Omega* **3**, 13952–13959 (2018).
45. Wang, X. *et al.* Multifunctional graphene quantum dots for simultaneous targeted cellular imaging and drug delivery. *Colloids and Surfaces B: Biointerfaces* **122**, 638–644 (2014).
46. PubChem. Graphene quantum dot. https://pubchem.ncbi.nlm.nih.gov/compound/146000141.
47. Dadvand, M. & Savadogo, O. Effect of hBN on Corrosion and Wear Performances of DC Electrodeposited NiW and NiW–SiC on Brass Substrates. *Coatings* **12**, 1011 (2022).
48. Shulpekova, Y. *et al.* The Concept of Folic Acid in Health and Disease. *Molecules* **26**, 3731 (2021).
49. Baker, M. J. *et al.* Using Fourier transform IR spectroscopy to analyze biological materials. *Nat Protoc* **9**, 1771–1791 (2014).

50. Bressi, V., Ferlazzo, A., Iannazzo, D. & Espro, C. Graphene Quantum Dots by Eco-Friendly Green Synthesis for Electrochemical Sensing: Recent Advances and Future Perspectives. *Nanomaterials* **11**, 1120 (2021).
51. Mahesh, S., Lekshmi, C. L., Renuka, K. D. & Joseph, K. Simple and Cost-Effective Synthesis of Fluorescent Graphene Quantum Dots from Honey: Application as Stable Security Ink and White-Light Emission. *Particle & Particle Systems Characterization* **33**, 70–74 (2016).
52. Rueden, C. T. *et al.* ImageJ2: ImageJ for the next generation of scientific image data. *BMC Bioinformatics* **18**, 529 (2017).
53. Zhang, S. & Wang, C. Precise Analysis of Nanoparticle Size Distribution in TEM Image. *Methods and Protocols* **6**, 63 (2023).
54. Shtansky, D. V. *et al.* Recent Progress in Fabrication and Application of BN Nanostructures and BN-Based Nanohybrids. *Nanomaterials (Basel)* **12**, 2810 (2022).
55. Patri, A. *et al.* Energy dispersive X-ray analysis of titanium dioxide nanoparticle distribution after intravenous and subcutaneous injection in mice. *Journal of Applied Toxicology* **29**, 662–672 (2009).
56. Zheng, J., Nagashima, K., Parmiter, D., de la Cruz, J. & Patri, A. K. SEM X-ray microanalysis of nanoparticles present in tissue or cultured cell thin sections. *Methods Mol Biol* **697**, 93–99 (2011).
57. Williams, D. B. & Carter, C. B. Scattering and Diffraction. in *Transmission Electron Microscopy: A Textbook for Materials Science* (eds. Williams, D. B. & Carter, C. B.) 23–38 (Springer US, Boston, MA, 2009). doi:10.1007/978-0-387-76501-3_2.

58. Kumawat, M. K., Thakur, M., Gurung, R. B. & Srivastava, R. Graphene Quantum Dots for Cell Proliferation, Nucleus Imaging, and Photoluminescent Sensing Applications. *Sci Rep* **7**, 15858 (2017).
59. Zhai, L. *et al.* Cyanate ester resin based composites with high toughness and thermal conductivity. *RSC Advances* **9**, 5722–5730 (2019).
60. Sudeep, P. M. *et al.* Functionalized boron nitride porous solids. *RSC Adv.* **5**, 93964–93968 (2015).
61. Wovchko, E. A., Yates, J. T., Scheithauer, M. & Knözinger, H. Reducing Radiation Damage in Raman Spectroscopy of Powdered Materials. *Langmuir* **14**, 552–555 (1998).
62. Dąbrowska, A. K. *et al.* Two stage epitaxial growth of wafer-size multilayer h-BN by metal-organic vapor phase epitaxy – a homoepitaxial approach. *2D Mater.* **8**, 015017 (2020).
63. Chong, Y. *et al.* The in vitro and in vivo toxicity of graphene quantum dots. *Biomaterials* **35**, 5041–5048 (2014).
64. Ahina, K. M. *et al.* Zero dimensional Graphene Quantum Dots self-assembled collagen 3D bio-matrices for soft tissue regeneration. *Materials Today Communications* **37**, 107244 (2023).
65. Parin, F. N., Ullah, S., Yildirim, K., Hashmi, M. & Kim, I.-S. Fabrication and Characterization of Electrospun Folic Acid/Hybrid Fibers: In Vitro Controlled Release Study and Cytocompatibility Assays. *Polymers* **13**, 3594 (2021).

66. Li, R., Wang, X., Li, Z., Zhu, H. & Liu, J. Folic acid-functionalized graphene quantum dots with tunable fluorescence emission for cancer cell imaging and optical detection of Hg 2+. *New Journal of Chemistry* **42**, 4352–4360 (2018).
67. Baibarac, M., Smaranda, I., Nila, A. & Serbschi, C. Optical properties of folic acid in phosphate buffer solutions: the influence of pH and UV irradiation on the UV-VIS absorption spectra and photoluminescence. *Sci Rep* **9**, 14278 (2019).
68. Castillo, J. J., Rindzevicius, T., Rozo, C. E. & Boisen, A. Adsorption and Vibrational Study of Folic Acid on Gold Nanopillar Structures Using Surface-Enhanced Raman Scattering Spectroscopy. *Nanomaterials and Nanotechnology* **5**, 29 (2015).
69. Verdin, A., Sloan-Dennison, S., Malherbe, C., Graham, D. & Eppe, G. SERS nanotags for folate receptor α detection at the single cell level: discrimination of overexpressing cells and potential for live cell applications. *Analyst* **147**, 3328–3339 (2022).
70. Hu, P. *et al.* β2-adrenergic receptor activation promotes the proliferation of A549 lung cancer cells via the ERK1/2/CREB pathway. *Oncology Reports* **36**, 1757–1763 (2016).
71. Senol, S. *et al.* Folate receptor α expression and significance in endometrioid endometrium carcinoma and endometrial hyperplasia. *Int J Clin Exp Pathol* **8**, 5633–5641 (2015).
72. Corsetti, S., Rabl, T., McGloin, D. & Nabi, G. Raman spectroscopy for accurately characterizing biomolecular changes in androgen-independent prostate cancer cells. *J Biophotonics* **11**, e201700166 (2018).

73. Pyrgiotakis, G. *et al.* Cell (A549)–Particle (Jasada Bhasma) interactions using Raman spectroscopy. *Biopolymers* **89**, 555–564 (2008).
74. Hanna, K. *et al.* Raman spectroscopy: current applications in breast cancer diagnosis, challenges and future prospects. *Br J Cancer* **126**, 1125–1139 (2022).
75. Elumalai, S., Managó, S. & De Luca, A. C. Raman Microscopy: Progress in Research on Cancer Cell Sensing. *Sensors (Basel)* **20**, 5525 (2020).
76. Hoshyar, N., Gray, S., Han, H. & Bao, G. The effect of nanoparticle size on in vivo pharmacokinetics and cellular interaction. *Nanomedicine (Lond)* **11**, 673–692 (2016).
77. Israelsen, N. D., Hanson, C. & Vargis, E. Nanoparticle Properties and Synthesis Effects on Surface-Enhanced Raman Scattering Enhancement Factor: An Introduction. *The Scientific World Journal* **2015**, 1–12 (2015).
78. Moskovits, M. Surface-enhanced Raman spectroscopy: a brief retrospective. *Journal of Raman Spectroscopy* **36**, 485–496 (2005).
79. Njoki, P. N. *et al.* Size Correlation of Optical and Spectroscopic Properties for Gold Nanoparticles. *J. Phys. Chem. C* **111**, 14664–14669 (2007).